

## **Structure-based discovery of cannabinoid-1 receptor agonists with reduced side effects**

Tia A. Tummino<sup>1,2,†</sup>, Christos Iliopoulos-Tsoutsouvas<sup>3,†</sup>, Joao M. Braz<sup>4,†</sup>, Evan S. O'Brien<sup>5</sup>, Reed M. Stein<sup>1,2</sup>, Veronica Craik<sup>4</sup>, Ngan K. Tran<sup>3</sup>, Suthakar Ganapathy<sup>3</sup>, Yuki Shiimura<sup>5,6</sup>, Fei Tong<sup>3</sup>, Thanh C. Ho<sup>3</sup>, Dmytro S. Radchenko<sup>7</sup>, Yurii S. Moroz<sup>8,9</sup>, Fangyu Liu<sup>1</sup>, Sian Rodriguez Rosado<sup>4</sup>, Karnika Bhardwaj<sup>4</sup>, Jorge Benitez<sup>4</sup>, Yongfeng Liu<sup>10</sup>, Herthana Kandasamy<sup>11</sup>, Claire Normand<sup>11</sup>, Meriem Semache<sup>11</sup>, Laurent Sabbagh<sup>11</sup>, Isabella Glenn<sup>1</sup>, John J. Irwin<sup>1</sup>, Kaavya Krishna Kumar<sup>5,\*</sup>, Alexandros Makriyannis<sup>3,12\*</sup>, Allan I. Basbaum<sup>4,\*</sup>, & Brian K. Shoichet<sup>1,\*</sup>

<sup>1</sup>Department of Pharmaceutical Chemistry, University of California, San Francisco, San Francisco, CA 94158, USA

<sup>2</sup>Graduate Program in Pharmaceutical Sciences and Pharmacogenomics, University of California, San Francisco, San Francisco, CA 94158, USA

<sup>3</sup>Center for Drug Discovery and Department of Pharmaceutical Sciences, Northeastern University, Boston, MA 02115, USA

<sup>4</sup>Department of Anatomy, University of California, San Francisco, San Francisco, CA 94158, USA

<sup>5</sup>Department of Molecular and Cellular Physiology, Stanford University School of Medicine, Stanford, CA 94305, USA

<sup>6</sup>Division of Molecular Genetics, Institute of Life Science, Kurume University, Fukuoka, Japan

<sup>7</sup>Enamine Ltd., 67 Chervonotkatska Street, Kyiv, 02094, Ukraine

<sup>8</sup>National Taras Shevchenko University of Kyiv, 60 Volodymyrska Street, Kyiv 01601, Ukraine

<sup>9</sup>Chemspace LLC, 85 Chervonotkatska Street, Suite 1, Kyiv, 02094, Ukraine

<sup>10</sup>National Institute of Mental Health Psychoactive Drug Screening Program (NIMH PDSP), School of Medicine, University of North Carolina at Chapel Hill School of Medicine, Chapel Hill, NC 27599, USA

<sup>11</sup>Domain Therapeutics North America Inc., Montréal, Québec, H4S 1Z9, Canada, Montréal, QC, H3T 1J4, Canada

<sup>12</sup>Department of Chemical and Chemical Biology, Northeastern University, Boston, MA 02115, USA

†These authors contributed equally.

\*Corresponding authors: [kaavyak@stanford.edu](mailto:kaavyak@stanford.edu), [a.makriyannis@northeastern.edu](mailto:a.makriyannis@northeastern.edu), [allan.basbaum@ucsf.edu](mailto:allan.basbaum@ucsf.edu), [bshoichet@gmail.com](mailto:bshoichet@gmail.com)

## Abstract

Docking tangible virtual libraries can reveal unexpected chemotypes that complement the structures of biological targets. Seeking new agonists for the cannabinoid-1 receptor (CB1R), we docked 74 million tangible molecules, prioritizing 46 high ranking ones for *de novo* synthesis and testing. Nine were active by radioligand competition, with > 50% radioligand displacement, a 20% hit-rate. Structure-based optimization of one of the most potent of these ( $K_i = 731$  nM) led to **'3234**, a 1.9 nM binder and a full CB1 agonist. A cryo-EM structure of the **'3234**-CB1- $G_{i1}$  complex confirmed its docked pose, providing a template for further optimization. The new agonist was strongly analgesic especially against thermal pain, with a 10-fold therapeutic window over sedation and no observable catalepsy or conditioned place preference or aversion. These findings suggest that new cannabinoid chemotypes may be able to disentangle the characteristic “tetrad” side-effects from its desired analgesic effect, supporting the further development of cannabinoids as pain therapeutics.

## Introduction

Although the therapeutic use of cannabinoids dates back to at least the 15<sup>th</sup> century<sup>1,2</sup>, their use in modern therapy, for instance as analgesics, has been slowed by their sedative and mood-altering effects, and by concerns over their reinforcing and addictive properties<sup>3,4</sup>. With changes in cannabis' legal status, an ongoing epidemic of chronic pain, as well as an effort to reduce reliance on opioids for pain management, has come a renewed interest in understanding both the endocannabinoid system and how to leverage it for therapeutic development<sup>5</sup>. Areas of potential application include anxiety<sup>6</sup>, nausea<sup>7</sup>, obesity<sup>8</sup>, seizures<sup>9</sup>, and pain<sup>10</sup>, the latter of which is the focus of this study. Progress in these areas has been slowed by the physical properties of the cannabinoids themselves, which are often highly hydrophobic, by the challenges of the uncertain legal environment, and by the substantial adverse side effects often attending on cannabinoids, including sedation, psychotropic effects, and concerns about reinforcement and addiction<sup>3</sup>. Indeed, a characteristic defining feature of cannabinoids is their “tetrad” of effects<sup>11</sup>: analgesia, hypothermia, catalepsy, and hypolocomotion, the latter three of which may be considered adverse. Additionally, inconclusive results in human clinical trials<sup>12</sup> have led to uncertainty in the field as to the effectiveness of cannabinoids as therapeutics. Nevertheless, the strong interest in new analgesics, and the clear efficacy of cannabinoids in animal models of nociception<sup>13</sup>, have maintained therapeutic interest in these targets.

The cannabinoid-1 and -2 receptors (CB1R and CB2R), members of the lipid family of G-protein coupled receptors (GPCRs), are the primary mediators of cannabinoid

activity<sup>14</sup>. The structural determination of these receptors<sup>15–21</sup> affords the opportunity to use structure-based methods to find ligands with new chemotypes. Recent structure-based docking of make-on-demand virtual libraries have discovered new chemotypes for a range of targets, often with new pharmacology and reduced side effects<sup>22–28</sup>. Thus, new CB1R chemotypes might address some of the unfavorable properties of current cannabinoids, such as their physicochemical properties or side-effect profiles. To identify such new chemotypes, we computationally docked a library of 74 million virtual but readily accessible (“tangible”) molecules against CB1R, revealing a range of new scaffolds with favorable physical properties. Structure-based optimization led to agonists binding with low-nanomolar binding affinities. The lead agonist is a potent analgesic, with pain-relieving activity at doses as low as 0.1 mg/kg. It has a ten-fold separation between analgesia and sedation with no observable catalepsy at analgesic doses, addressing two of the four aspects of the “tetrad” and highlighting the utility of large-scale virtual screening for identifying unique biology through new chemistry.

## Results

***Large-library docking against CB1R.*** The CB1R orthosteric site is large and lipophilic, explaining the high molecular weight and hydrophobicity of many of its ligands (**Extended Data Fig. 1**), which are metabolic and solubility liabilities<sup>29</sup>. We therefore sought molecules in a more “lead-like” physical property range. In preliminary studies, strict enforcement of such properties (i.e.,  $MW \leq 350$  amu,  $cLogP \leq 3.5$ ) revealed no new



ligands from docking. Accordingly, we created a special 74-million molecule subset of the ZINC15 database<sup>30</sup> composed of molecules 350 to  $\geq 500$  amu and calculated LogP (cLogP) 3 to  $\leq 5$ , reasoning that these would be more likely to complement the CB1R site, while still being more polar and smaller than typical of cannabinoid ligands (**Fig. 1B**). Each molecule was docked in an average of 3.04 million poses (orientations x conformations), totaling roughly 63 trillion sampled and scored complexes. Seeking a diverse set of molecules to test, the top-ranking 300,000 were clustered into 60,420 sets, and the highest scoring member of each cluster was filtered for topological dissimilarity to known CB1/CB2 receptor ligands in ChEMBL<sup>31,32</sup>. High-ranking library compounds that did not resemble known ligands ( $T_c < 0.38$ ) were filtered for potential polar interactions with S383<sup>7,39</sup>, and H178<sup>2,65</sup> (superscripts denote Ballesteros-Weinstein nomenclature<sup>33</sup>; see **Methods, Fig. 1A, Supplementary Table 1**). The top-ranking 10,000 remaining molecules were visually evaluated in UCSF Chimera<sup>34</sup>, and 60 were prioritized for *de novo* synthesis. Of these, 46 were successfully made and tested for CB1R activity. Consistent with the design of the library, the new molecules were smaller and more polar than most existing cannabinoid ligands, skirting the edge of property-space that is suitable for the large and hydrophobic CB1 orthosteric pocket (**Fig. 1B**).

In single-point radioligand displacement experiments, nine of the 46 prioritized molecules displaced over 50% of the radioligand, a 20% hit-rate (**Fig. 1C-D, Supplementary Table 1**). The top four of these (ZINC537551486, ZINC1341460450, ZINC749087800, and ZINC518437019, referred to as ‘**51486**’, ‘**0450**’, ‘**7800**’, and ‘**7019**’, respectively, from here on) were then tested in full concentration-response. All four

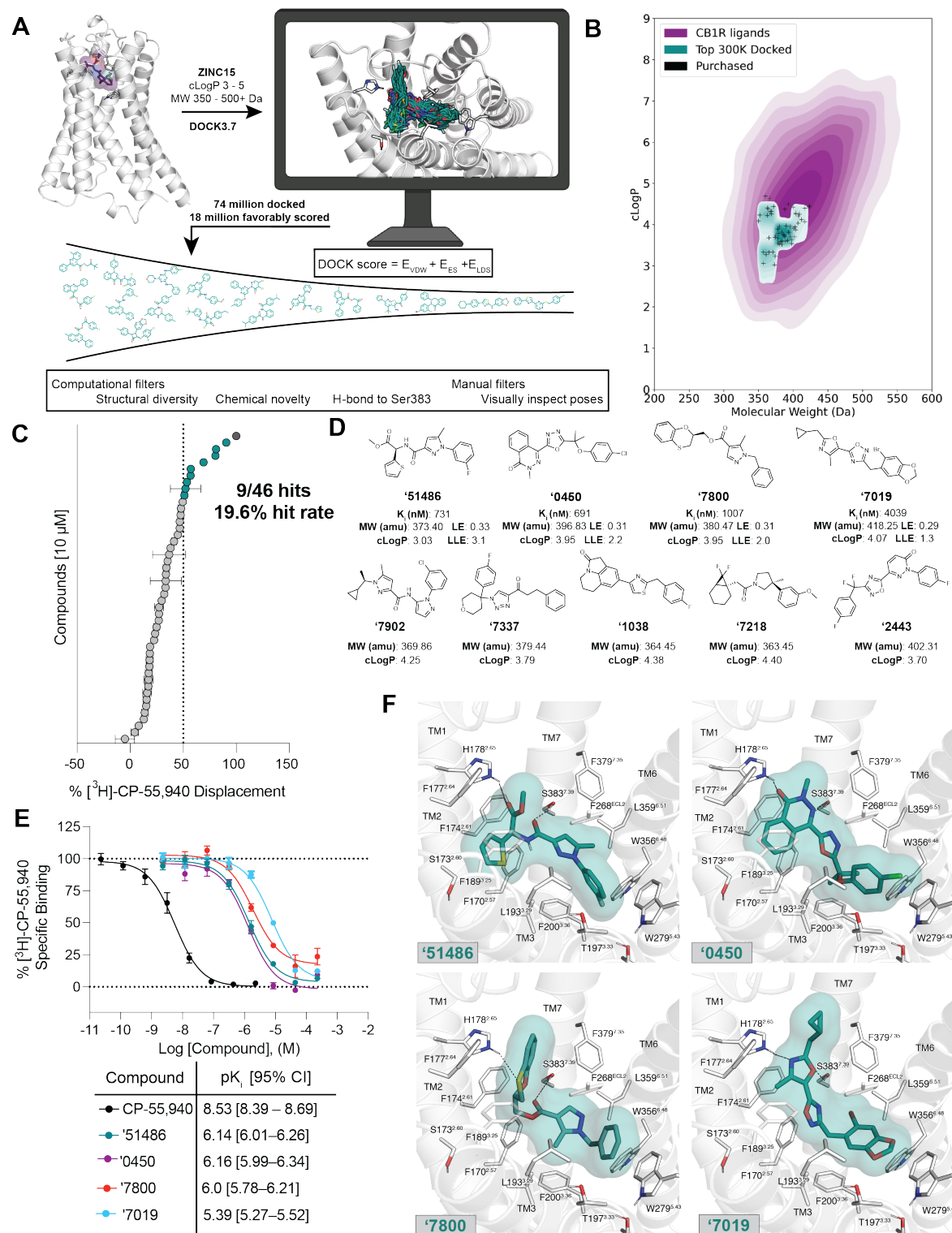


**Figure 1. Large-scale docking of a 74-million molecule library against the CB1R. A.** Workflow of the docking campaign. **B.** Overlap of physical properties of CB1R ligands versus the top docked and purchased ligands. **C.** Single-point radioligand displacement data for the 46 tested compounds. **D.** 2D structures and properties of the nine hits. **E.** Secondary binding assay for the top four hits. **F.** Docked poses of the top four hits with H-bonds and other binding pocket residues indicated. Data in panels **C.** and **E.** represent mean  $\pm$  SEM from three independent experiments.

displaced the radioligand  $^3\text{H}$ -CP-55,940, with  $K_i$  values ranging from  $\sim 700$  nM to  $4\text{ }\mu\text{M}$  (**Fig. 1E**). Owing to coupling to the inhibitory  $G_{\text{ai}}$  G-protein, functional efficacy experiments monitoring a decrease in forskolin (FSK) simulated cAMP were tested using hCB1-expressing cells, with **'51486** and **'0450** showing modest agonist activity. Limited solubility prohibited testing at high enough concentrations to obtain accurate  $\text{EC}_{50}$  measurements; fortunately, colloidal aggregation counter-screens showed no such activity below  $10\text{ }\mu\text{M}$  (**Extended Data Fig. 2**). Taken together, the nine actives explore a range of chemotypes topologically unrelated to known CB1 ligands, with relatively favorable physical properties.

Although the new ligands are chemically and physically distinct from established cannabinoids; their docked poses recapitulate the interactions of the known ligands but do so with different scaffold and recognition elements. All of the four most potent ligands docked to adopt the “C” shaped conformation characteristic of the experimentally observed geometries of MDMB-Fubinaca<sup>18</sup>, AM11542, and AM841<sup>16</sup> bound to CB1R. Similarly, all four are predicted to hydrogen-bond with S383<sup>7,39</sup>, a potency-determinant interaction at CB1 receptors observed in all agonist-bound ligand-receptor complexes<sup>35</sup>. Additionally, all four ligands are predicted to make secondary hydrogen bonds to H178<sup>2,65</sup>, a feature seen in only the most potent CB1 ligands, such as MDMB-Fubinaca. Largely, these electrostatic interactions are made using unique hydrogen-bond acceptor groups, such as an oxazole, oxathiine, or pyridazinone. Other characteristic hydrophobic and aromatic stacking interactions are found throughout the ligands, including with F268<sup>ECL2</sup>, W279<sup>5,43</sup>, and F174<sup>2,61</sup>, though again often using different aromatic groups than found in

the known ligands (**Fig. 1F**). Similarly, all four ligands exhibit aromatic stacking and hydrophobic packing with the twin-toggle switch residues W356<sup>6,48</sup> and F200<sup>3,36</sup> which are important for receptor activation<sup>36,37</sup>.

We sought to optimize these initial ligands. Molecules with ECFP4 Tcs  $\geq 0.5$  to the four actives were sought among a library of 12 billion tangible molecules using SmallWorld (NextMove Software, Cambridge UK), a program well-suited to ultra-large libraries. These analogs were built, docked, filtered, and selected using the same criteria as in the original docking campaign. Between 11 and 30 analogs were synthesized for each of the four scaffolds. Optimized analogs were found for three of the four initial hits, improving affinity by between 5 and 24-fold, with ‘**51486**’ improving 16-fold to a  $K_i$  of 44 nM, ‘**7019**’ improving 5-fold to 87 nM, and ‘**0450**’ improving 24-fold to 163 nM (**Supplementary Table 2**). In subsequent bespoke synthesis, the 44 nM analog of ‘**51486**’, ‘**60154**’, was further optimized to compound Z4971163234 (from here on referred to as ‘**3234**’) with a  $K_i$  of 1.9 nM (**Extended Data Fig. 3**). **Figure 2** summarizes the structure-activity relationship (SAR) of the ‘**51486**’/‘**3234**’ series.

Key learnings from the SAR include the importance of a hydrophobic group in the  $R_1$  position of ‘**3234**’, which is modeled to pack against W279<sup>5,43</sup> and T197<sup>3,33</sup> in CB1R. They also include methylation of the linking amide nitrogen ( $R_4$  position), which has no nearby polar receptor group to complement it, theoretically reducing its desolvation penalty. Finally, the terminal ester is modeled to hydrogen bond with H178<sup>2,65</sup> of the receptor. Concerned that it might be a hydrolysis liability, we sought replacements that

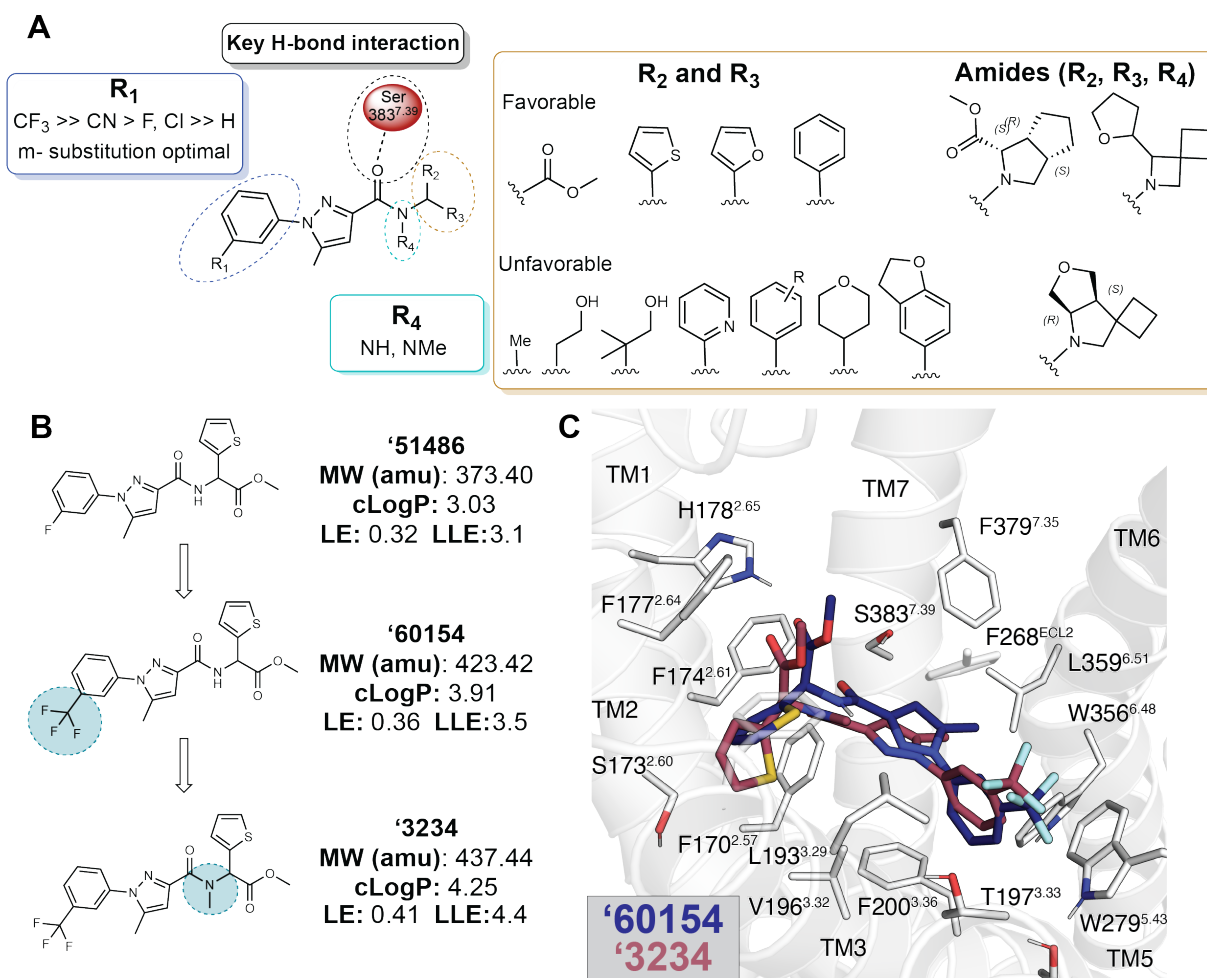


**Figure 2. Structure-activity relationships and optimization of '51486 to '3234. A.** Pharmacophore model based on the structure-activity relationships discovered via analoging '51486. **B.** 2D structures of the docking hit '51486 and analogs that lead to '3234. **C.** Docking predicted pose of '60154 (navy) and '3234 (purple).

might preserve the hydrogen bond while increasing stability. However, both acetyl substitutions ('6829) and ligands with a furan bioisostere ('1090, '4388) lost substantial affinity (Supplementary Table 2). As expected, the carboxylate analog of the ester, '9056, was a weak binder ( $K_i = 5 \mu\text{M}$ , 5,000-fold less potent)—this molecule, a very close analog to '3234, may provide the inactive member of a “probe pair” for future research. The lead that emerged, '3234 at 1.9 nM, is about 2-fold more potent than the widely used CB1R probe CP-55,940 (Fig. 4B, below) and equipotent to the marketed drug nabilone

(**Extended Data Fig. 3A, Supplementary Table 2**). Although its cLogP is higher than the docking hit **'51486**, its lipophilic ligand efficiency improved from 3.1 to 4.4 (**Fig. 2B**).

**Cryo-EM structure of the '1066-CB1R-G<sub>i1</sub> complex.** To understand the SAR of the **'3234** series at atomic resolution, and to template future optimization, we determined the structure of the agonist in complex with the activated state of the receptor. Initial efforts at single particle cryo-electron microscopy (cryo-EM) of **'3234** in complex with CB1R and the G<sub>i1</sub> heterotrimeric G-protein led to a structure where the ligand density seemed to reflect either multiple conformations of a single ligand, or multiple ligands. As **'3234** is a racemate, we purified it into its component isomers, **'1066** and **'6000** using chiral chromatography (**Extended Data Fig. 4**) and measured CB1R binding by radioligand competition, as above. With K<sub>i</sub> values of 0.95 nM and 90 nM, respectively, **'1066** was substantially more potent than its enantiomer, and subsequent functional studies revealed it to be the much stronger agonist (**Fig. 4A-B, Extended Data Fig. 4**; below). Accordingly, we re-determined the cryo-EM structure of the **'1066-CB1R-G<sub>i1</sub> complex (Fig. 3, Extended Data Fig. 5, see Methods)** to a nominal resolution of 3.3 Å (**Supplementary Table 3**). Consistent with earlier structures of CB1R in its activated state, the ligand occupies the orthosteric pocket formed by transmembrane helices (TMs) 2-3 and 5-7 and is capped by extracellular loop (ECL) 2.

The experimental structure of **'1066** superposes well on the docking-predicted pose of **'3234** in its *R*-enantiomer, which was the enantiomer with the better docking score to the receptor (-33 DOCK score versus -29 DOCK score for the *S*-enantiomer). The



predicted and experimental structures superposed with an all-atom RMSD of 1.5 Å (**Fig. 3B**). The major interactions with CB1R predicted by the docking are preserved in the experimental structure, including the key hydrogen-bond between the amide carbonyl of the ligand and S383<sup>7.39</sup>. The trifluoromethyl group is complemented by van der Waals and quadrupole interactions with residues W279<sup>5.43</sup> and T197<sup>3.33</sup>, as anticipated by the docked structure, and consistent with the improvement in affinity by -1.7 kcal/mol (17-fold in  $K_i$ ) on its replacement of the original fluorine. Similarly, the amide nitrogen of the agonist in the experimental structure is not nearby any polar group on the receptor, consistent with the impact of its methylation in the SAR series, which presumably reduces desolvation penalties and improves affinity by -1.9 kcal/mol (24-fold in  $K_i$ ). The major difference between the docked pose of ‘1066 and the cryogenic pose is the placement

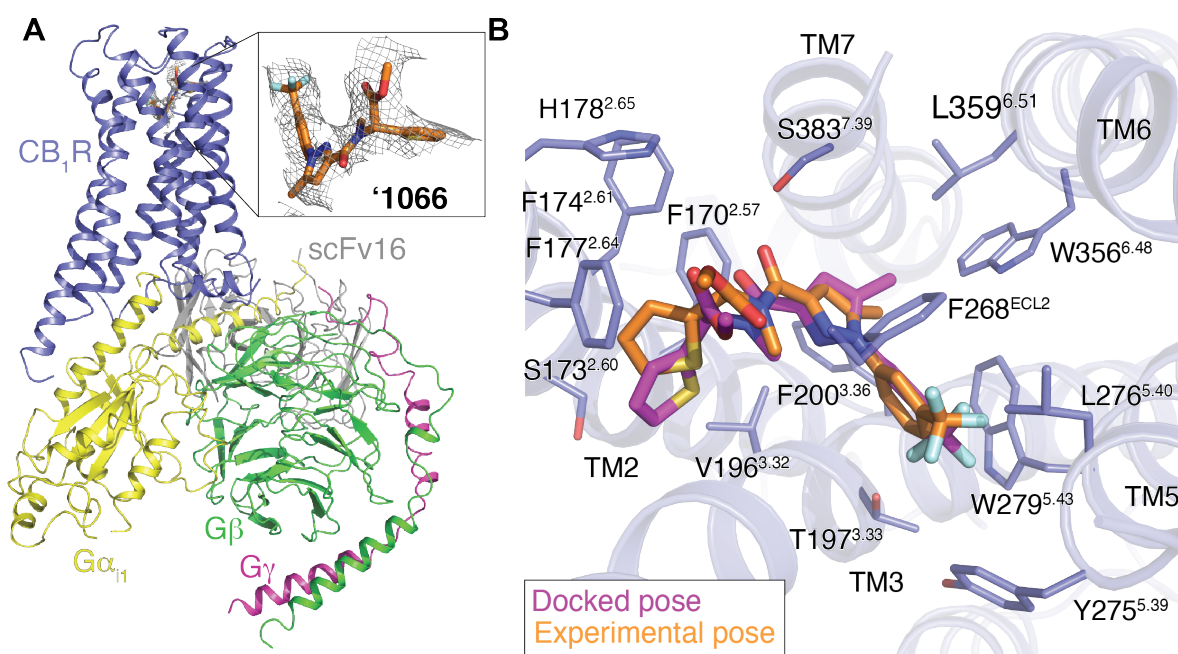


**Figure. 3 Cryo-EM structure of ‘1066-CB1R-Gi1 complex.** **A.** Cryo-EM structure of ‘1066-CB1R-Gi1 highlighting the ligand density. **B.** Overlay of the docked pose (magenta) with the experimental pose (orange) of ‘1066.

of the methyl ester, where the docked pose predicts the carbonyl to make a secondary hydrogen bond to H178<sup>2,65</sup> while in the experimental pose it is instead the ester oxygen that orients toward H178<sup>2,65</sup>. This feature may explain the weak activity of the acetyl analog (**'6829**), which to our surprise was >500-fold less active than the ester counterpart (**Extended Data Fig. 3A**).

**Agonism and subtype selectivity of '3234.** Given the potent affinity of **'3234** and of **'1066 (Fig. 4A)**, we next investigated their functional activity, and how they compared to that of the widely studied cannabinoid, CP-55,940<sup>2</sup>. We first measured G<sub>i/o</sub> mediated agonism via inhibition of forskolin-stimulated cAMP in the Lance Ultra cAMP assay (see **Methods**). Both **'3234**, **'1066**, and several of its analogs are agonists in human CB1R-expressing cells (hCB1R), with EC<sub>50</sub> values commensurate with their affinities (**Supplementary Table 2,4 Extended Data Fig. 3,6-7**) and with efficacies close to full agonism (E<sub>max</sub> typically > 75%). **'3234** and **'1066** had hCB1R EC<sub>50</sub> (E<sub>max</sub>) values of 3.3 nM (78%) and 1.6 nM (77%) (**Fig. 4B**). The activity of racemic **'3234** was confirmed in several orthogonal cAMP and β-Arrestin assays (see **Methods**), including in the Cerep cAMP assay (**Extended Data Fig. 3C**), the Glosensor assay (**Extended Data Fig. 3D**), the Tango β-Arrestin translocation assay (**Extended Data Fig. 3E**) and the DiscoverX β-Arrestin-2 recruitment assay (**Extended Data Fig. 3F**). In summary, **'3234** and its *R*-isomer, **'1066**, are potent agonists of hCB1R with low nM EC<sub>50</sub> values.

Fortified by this potent activity, and to control for system bias<sup>38–40</sup>, we investigated both **'3234** and the more active of its stereoisomers, **'1066**, for differential recruitment of



several G-proteins and  $\beta$ Arrestin-2 against both CB1R and CB2R in the ebBRET bioSens-All® platform, comparing its activity to CP-55,940 (Fig. 4C-F, Extended Data Fig. 6, Supplementary Table 5-6). A good way to picture its differential effects, versus both CP-55,940 and comparing CB1R to CB2R, is via “radar” plots (Fig. 4C and 4E). In CB1R, ‘1066 was approximately 2 times more efficacious at recruiting  $G_{i/o}$  subtypes than CP-55,940, though the pattern of effectors recruited was similar (see **Methods**). Similar coupling profiles were seen for ‘3234, though the effects were smaller, consistent with the latter compound being an enantiomeric mixture. Whereas the CB1R radar plots were similar in pattern for ‘1066, ‘3234 and CP-55,940, the differential activities for the highly

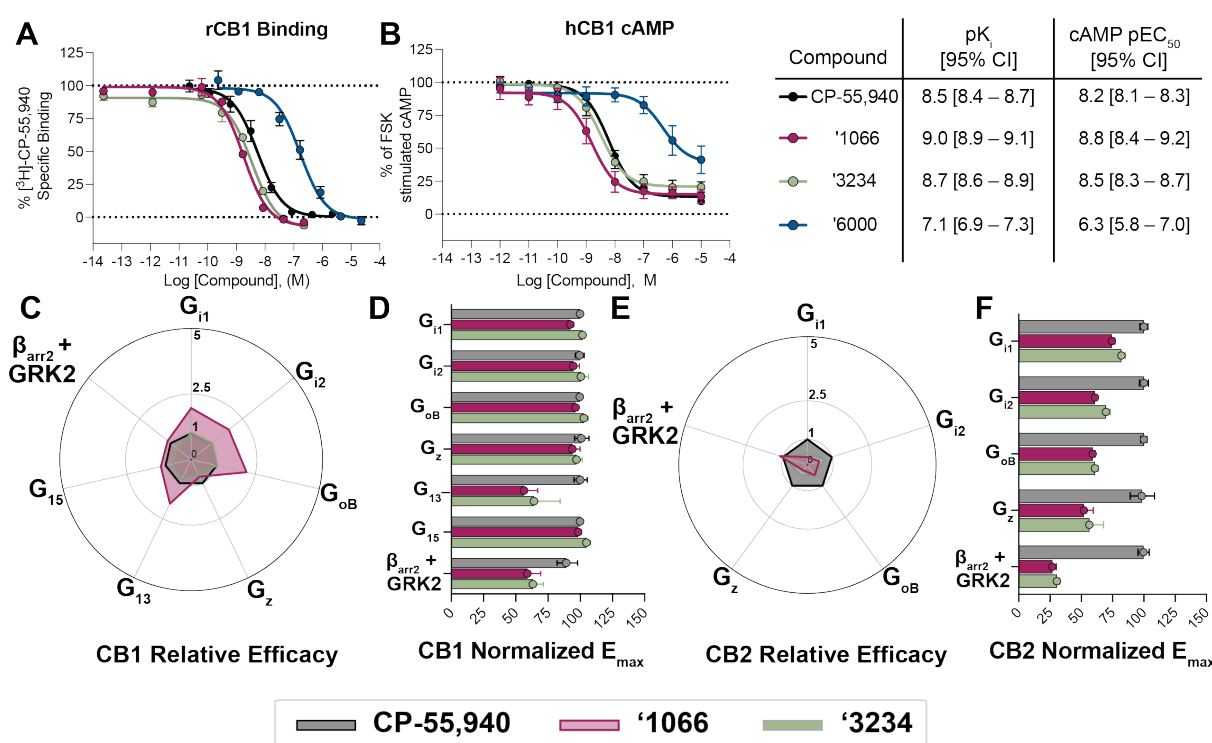


**Figure 4. Functional activity of ‘3234 and its active enantiomer ‘1066.** **A.** Binding affinity of ‘3234 and its enantiomers ‘1066 and ‘6000 at rCB1. **B.** Functional cAMP inhibition by ‘3234 and its enantiomers ‘1066 and ‘6000. **C.** Relative efficacy of ‘1066 and ‘3234 compared to CP-55,940 at hCB1. **D.** Normalized  $E_{max}$  from the experiments in **C.** **E.** Relative efficacy of ‘1066 and ‘3234 compared to CP-55,940 at hCB2. **F.** Normalized  $E_{max}$  from the experiments in **E.** Data in **A.** & **B.** represent mean  $\pm$  SEM from three independent experiments. Data in **D** & **F.** represent mean  $\pm$  95% CI from two to four independent experiments.

related CB2R differed qualitatively (**Fig. 4E-F; Extended Data Fig. 6; Supplementary Table 7-8**). Although the affinity of **'3234** at the two receptors is almost undistinguishable (**Extended Data Fig. 8**), there was a marked difference in functional activity, with **'3234** consistently being a weaker efficacy partial agonist at CB2R (**Extended Data Fig. 6C-D, 8**) versus its essentially full agonism at CB1. This was true for the racemate **'3234** as well as its active enantiomer **'1066** across four separate functional assays including the bioSens-Air® BRET assay, the Lance Ultra cAMP assay, TRUPATH BRET2 assay, and the Tango  $\beta$ -Arrestin recruitment assay (**Extended Data Fig. 8B-D**). Indeed, whereas against CB1R **'1066/ R-'3234** had greater relative efficacy against inhibitory G-proteins versus CP-55,940, in CB2R the pattern was reversed, with CP-55,940 being substantially more efficacious than **'1066/ R-'3234** (**Fig. 4C-F**).

***The new CB1R agonist is analgesic with reduced cannabinoid side effects.***

**Off-target selectivity and pharmacokinetics.** Encouraged by the potency and functional selectivity, and the negligible functional differences between the racemic and enantiomeric mixture, we progressed **'3234** into *in vivo* studies for pain relief. We began by investigating the selectivity of **'3234** against potential off-targets. **'3234** was tested first for binding and functional activity against a panel of 320 GPCRs and 46 common drug targets at the PDSP (**Extended Data Fig. 9**). Little activity was seen except against the melatonin-1 (MT1R), ghrelin (GHSR), Sigma 1 and peripheral benzodiazepine receptors. In secondary validation assays, only weak partial agonism was observed against these receptors, with EC<sub>50</sub> values greater than 1  $\mu$ M (**Extended Data Fig. 9**), 1,000-fold weaker than CB1R. Intriguingly, no agonist activity was seen for the putative cannabinoid

receptors GPR55, GPR18, or GPR119. Taken together, '**3234** appears to be selective for CB1 and CB2 receptors over many other integral membrane receptors.

To minimize locomotor effects in pharmacokinetic exposure experiments, we used a dose of 0.2 mg/kg (**Extended Data Fig. 10A**). At low dose, '**3234** was found appreciably in brain and plasma, but not CSF compartments, with higher exposure in brain tissue ( $AUC_{0 \rightarrow \infty} = 3180 \text{ ng} \cdot \text{min/mL}$ ) than plasma ( $AUC_{0 \rightarrow \infty} = 1350 \text{ ng} \cdot \text{min/mL}$ ). The molecule achieved concentrations in the brain ( $C_{\max} = 16.8 \text{ ng/g}$  or approximately 38 nM) and plasma ( $C_{\max} = 5.14 \text{ ng/mL}$  or 12 nM) at this dose. Assuming linear exposures with dosing, this suggests that in the anti-nociception assays (below) that '**3234** reaches concentrations 20- to 100-fold higher in the brain than its affinity for CB1R at times that are feasible for *in vivo* efficacy experiments ( $T_{\max}$  between 15-30 min). Importantly, the concentration of '**3234** needed to activate the identified off-target receptors even partially is about 10,000-fold higher than these concentrations, suggesting that activity seen *in vivo* with this ligand reflect on-target engagement.

**Anti-allodynia and analgesia.** Given its favorable exposure, we next tested the efficacy of '**3234** *in vivo*, in models of pain and inflammation. We first focused on acute thermal pain. In both tail flick and Hargreaves tests of thermal hypersensitivity, '**3234** increased both tail flick and paw withdrawal latencies in a dose-dependent fashion, showing significant analgesia, namely thresholds above baseline, at as little as 0.1 mg/kg dosed intraperitoneally (i.p.) (**Fig. 5A-B**). A similar analgesic effect was observed for the positive control ligand CP-55,940 at slightly higher 0.2 mg/kg doses in the Hargreaves

and tail flick tests. Next, we assessed the analgesic properties of **'3234** in the setting of inflammatory pain using the Complete Freund's Adjuvant (CFA) model. As illustrated in **Fig. 5C**, 0.2 mg/kg i.p. of **'3234** was not only anti-allodynic, but also analgesic, completely reversing the CFA-induced thermal hypersensitivity to well-above pre-CFA baseline levels.

We next tested the therapeutic potential of **'3234** in the spared nerve injury (SNI) model of neuropathic pain. In contrast to its strong anti-hyperalgesic effect in inflammatory pain models, at 0.2 mg/kg i.p. **'3234** was without effect in SNI mice (**Extended Data Fig. 10B-C**) but did have a modest anti-allodynic when dosed intrathecally (i.t.; up to 100 µg/kg; **Extended Data Fig. 10D-E**), suggesting weak effects on mechanical hypersensitivity consistent with literature reports for other CB1R agonists<sup>41–43</sup>. Furthermore, **'3234** did not alter the mechanical thresholds of naïve (non-SNI) animals dosed i.p. at 0.2 mg/kg (**Extended Data Fig. 10F**), a dose that was frankly analgesic in thermal pain assays. Conversely, **'3234** strongly reduced the SNI-induced cold allodynia, a hallmark of neuropathic pain, significantly decreasing the number of acetone-induced nocifensive behaviors, particularly for the paw withdrawals and paw shaking (**Fig. 5F**). Finally, in the formalin model of nociceptive pain, an i.p. administration of 0.2 mg/kg **'3234** produced a profound decrease in the duration of both phase 1 and phase 2 nocifensive behaviors (**Fig. 5E**) throughout the 60-minute observation period.

**On target activity: CB1R vs CB2R.** Consistent with CB1R being the target of **'3234** *in vivo*, pre-treatment with the CB1R selective antagonist AM251 (5.0 mg/kg)

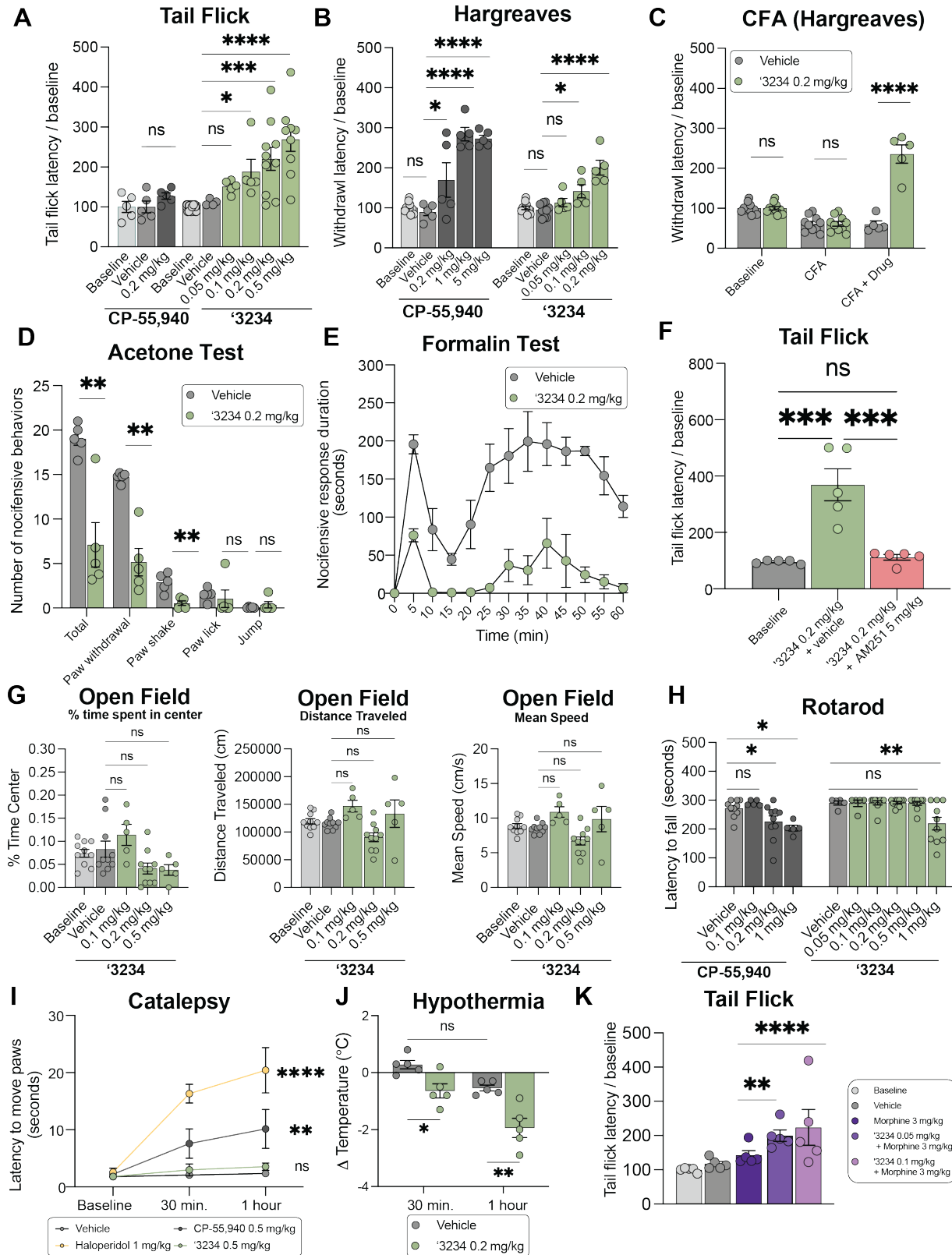


**Figure 5. In vivo analgesic and side-effect profile of ‘3234.** **A.** Dose-response activity in the tail flick assay for ‘3234 (0.05 and 0.1 mg/kg,  $n = 5$ ; 0.2 and 0.5 mg/kg  $n = 10$ ; one-way ANOVA,  $F(4, 54) = 18.5$ ,  $P < 0.0001$ ; asterisks define individual group differences to respective vehicle control using Dunnett’s multiple comparisons post-hoc test correction) and CP-55,940 ( $n = 5$ ; unpaired two-tailed  $t$ -test,  $t(8) = 1.62$ ,  $P > 0.05$ ). **B.** Dose-response activity in the Hargreaves assay for ‘3234 ( $n = 5$ ; one-way ANOVA,  $F(3, 21) = 16.26$ ,  $P < 0.0001$ ; asterisks define individual group differences to respective vehicle control using Dunnett’s multiple comparisons post-hoc test correction) and CP-55,940 ( $n = 5$ ; one-way ANOVA,  $F(4, 25) = 26.16$ ,  $P < 0.0001$ ; asterisks define individual group differences to respective vehicle control using Dunnett’s multiple comparisons post-hoc test correction). **C.** Hargreaves test of ‘3234 ( $n = 5$ ) after CFA treatment (two-way ANOVA; CFA x drug treatment interaction:  $F(2, 44) = 61.3$ ,  $P < 0.0001$ ; CFA:  $F(2, 44) = 50.7$ ,  $P < 0.0001$ ; drug treatment:  $F(1, 44) = 76.6$ ,  $P < 0.0001$ ; asterisks define individual group differences to vehicle control using Šídák’s multiple comparisons post-hoc test correction). **D.** Chemical hyperalgesia test after spared nerve injury (all  $n = 5$ ; multiple two-tailed unpaired  $t$ -tests, total:  $t(8) = 4.6$ ,  $P = 0.007$ ; paw withdrawal:  $t(8) = 6.2$ ,  $P = 0.001$ ; paw shake:  $t(8) = 4.5$ ,  $P = 0.007$ ; paw lick:  $t(8) = 0.4$ ,  $P > 0.05$ ; jump:  $t(8) = 0.8$ ,  $P > 0.05$ ; asterisks define differences to vehicle control after the Holm-Šídák multiple comparisons post-hoc test correction). **E.** Nocifensive response duration after formalin treatment ( $n = 5$ ; multiple two-tailed unpaired  $t$ -tests at each timepoint with the Holm-Šídák post-hoc test correction; all times  $*P < 0.05$  –  $****P < 0.0001$  except 0 min. and 15 min., not significant). **F.** Tail flick latency after co-treatment with the selective CB1 antagonist AM251 (all  $n = 5$ ; one-way ANOVA,  $F(2, 17) = 29.9$ ,  $P < 0.0001$ ; asterisks define individual group differences to baseline control after Tukey’s multiple comparisons post-hoc test correction). **G.** Dose-response of ‘3234 in the open-field test of hypolocomotion (0.1 and 0.5 mg/kg,  $n = 5$ ; 0.2 mg/kg  $n = 10$ ; one-way ANOVA,  $F(3, 26) = 4.0$ ,  $P = 0.02$ ; asterisks define individual group differences to vehicle control after Dunnett’s multiple comparisons post-hoc test correction). **H.** Rotarod test of sedation comparison of CP-55,940 (all  $n = 5$  except 0.2 mg/kg  $n = 10$ ; one-way ANOVA,  $F(4, 30) = 3.5$ ,  $P = 0.02$ ; asterisks define individual group differences to respective vehicle control after Dunnett’s multiple comparisons post-hoc test correction) to ‘3234 (all  $n = 10$  except 0.05 mg/kg  $n = 5$ ; one-way ANOVA,  $F(5, 44) = 6.2$ ,  $P = 0.002$ ; asterisks define individual group differences to respective vehicle control after Dunnett’s multiple comparisons post-hoc test correction). **I.** Mesh grip test of catalepsy comparison of CP-55,940 ( $n = 10$ ; two-way ANOVA; time x drug treatment interaction:  $F(2, 54) = 2.28$ ,  $P > 0.05$ ; time:  $F(2, 54) = 2.99$ ,  $P = 0.05$ ; drug treatment:  $F(1, 54) = 10.02$ ,  $P = 0.003$ ; asterisks define difference to respective vehicle control at 1 hr only), haloperidol ( $n = 5$ ; two-way ANOVA; time x drug treatment interaction:  $F(2, 24) = 8.7$ ,  $P = 0.002$ ; time:  $F(2, 24) = 15.7$ ,  $P < 0.0001$ ; drug treatment:  $F(1, 24) = 31.7$ ,  $P < 0.0001$ ; asterisks define difference to respective vehicle control at 1 hr only), and ‘3234 ( $n = 5$ ; two-way ANOVA; time x drug treatment interaction:  $F(2, 24) = 0.2$ ,  $P > 0.05$ ; time:  $F(2, 24) = 3.0$ ,  $P > 0.05$ ; drug treatment:  $F(1, 24) = 6.8$ ,  $P = 0.02$ ; asterisks define difference to respective vehicle control at 1 hr only). One representative vehicle control shown for simplicity. **J.** Change in body temperature after treatment with ‘3234 (all  $n = 5$ ; two-way ANOVA; time x drug treatment interaction:  $F(1, 16) = 1.0$ ,  $P > 0.05$ ; time:  $F(1, 16) = 22.4$ ,  $P = 0.0002$ ; drug treatment:  $F(1, 16) = 26.7$ ,  $P < 0.0001$ ; asterisks define individual group differences after Tukey’s multiple comparisons post-hoc test correction). **K.** Cotreatment of subthreshold morphine with ‘3234 on the tail flick test (all  $n = 5$ ; two-way ANOVA; single drug x polypharmacy interaction:  $F(2, 24) = 7.5$ ,  $P = 0.003$ ; single drug:  $F(2, 24) = 5.5$ ,  $P = 0.01$ ; polypharmacy treatment:  $F(1, 24) = 104.2$ ,  $P < 0.0001$ ; asterisks define cotreatment differences to morphine alone (3 mg/kg) using Dunnett’s multiple comparisons post-hoc test correction). For all statistical tests: ns, not significant,  $*P < 0.05$ ,  $**P < 0.01$ ,  $***P < 0.001$ ,  $****P < 0.0001$ . All data represent mean  $\pm$  SEM of 5-10 animals.



completely blocked the analgesic effect of **'3234** in the tail flick assay (**Fig. 5F**). In contrast, neither CB2R knockout nor co-treatment with the CB2-selective antagonist SR-144528 (1.0 mg/kg) decreased analgesic effects of **'3234** in the tail flick or Hargreaves assays (**Extended Data Fig. 10G-I**). We conclude that both the anti-allodynic and analgesic effects of **'3234** are CB1R, but not CB2R, dependent.

**Cannabinoid tetrad of behaviors.** The cannabinoid “tetrad” of behaviors is commonly used to assess CNS engagement of cannabinoid receptors by novel ligands<sup>11</sup>. In addition to analgesia, this suite of tests measures three common cannabinoid side-effects—hypothermia, catalepsy, and hypolocomotion—as hallmarks of CB1R agonism. Given the novel chemotypes discovered here, we also examined our lead **'3234**, for this panel of potential side-effects.

**Reduced “sedation” at analgesic doses.** Hypolocomotion, one of the four features of the tetrad, is a commonly assessed proxy for the key sedative side-effect of cannabinoids. Sedation is not only an important clinical adverse side effect of cannabinoids, but it also confounds preclinical reflex tests of analgesia, where unimpeded movement of a limb is the endpoint. Intriguingly, while mice treated with **'3234** appeared less active than those treated with vehicle, **'3234**-injected mice were not sedated (**Fig. 5G-H**). Not only would the mice promptly move when slightly provoked (touched, or their housing cylinders slightly disturbed), but in two quantitative assays of sedation, the open field and rotarod tests, we found no significant differences between **'3234**- and vehicle-treated animals at analgesic doses (**Fig. 5G**), although higher doses tended to decrease

their overall locomotor activity. Only at the highest (1.0 mg/kg) dose did we record some motor deficits in the rotarod test. In contrast, all analgesic doses tested for the positive control CP-55,940 caused motor impairment in the rotarod test (**Fig. 5H**). We conclude that **'3234** has a 10-fold therapeutic window for analgesia over sedation, in contrast with the typical cannabinoid CP-55,940, the analgesic effects of which are confounded by their concurrent motor side effects.

**'3234 does not induce catalepsy but does cause hypothermia.** To determine whether **'3234** induces a second member of the tetrad, catalepsy, we measured the latency **'3234**-injected mice to move all four paws when placed on a vertical wire mesh. As expected, mice injected with the non-cannabinoid control cataleptic, haloperidol, showed dramatic catalepsy (**Fig. 5I**). In contrast, and consistent with its lack of locomotor effects, **'3234** did not induce any observable cataleptic behavior, even at the highest analgesic dose (0.5 mg/kg). Meanwhile, CP-55,940 showed significantly longer latencies to move all four paws at both 30 minutes and 1-hour post-injection. Finally, **'3234** did significantly reduced skin temperature at the nape of the neck, at both 30- and 60-minutes post injection 0.2 mg/kg i.p.; **Fig. 5J**), suggesting it did trigger the fourth element of the tetrad, hypothermia.

**Pretreatment with '3234 increases the efficacy of morphine.** As **'3234** can induce strong analgesia with reduced side effects, we next asked whether co-treatment of **'3234** with morphine has additional pain-relieving properties. We combined low doses of **'3234** with morphine (3.0 mg/kg, i.p.) and tested the analgesic efficacy of the



combination vs morphine alone in the tail flick assay. As illustrated in **Fig. 5J**, mice co-injected with morphine (3.0 mg/kg, i.p.) and a non-analgesic (0.05 mg/kg) or a low (0.1 mg/kg) analgesic dose of '**3234** exhibited significantly longer tail flick latencies than did mice injected with morphine alone. This result suggests that the two molecules have at least an additive analgesic effect, consistent with previous studies on both CB1R and CB2R ligand polypharmacy with morphine<sup>44,45</sup>.

**The novel CB1R agonist is not rewarding.** A major limiting factor in an analgesic's clinical utility, particularly opioids, is the potential for misuse because of their intrinsic rewarding properties. To determine whether '**3234** exhibits comparable liabilities, we turned to the conditioned place preference (CPP) test in which mice learn to associate one chamber of the apparatus with a rewarding compound. If mice show a preference for the drug-paired chamber, then the compound is considered to be intrinsically rewarding. As expected, mice injected with morphine significantly increased their preference for the chamber associated with that drug (**Extended Data Fig. 10J**). Encouragingly, mice injected with '**3234** spent similar amounts of time in the '**3234**-paired or vehicle-paired chambers, indicating that '**3234** does not induce CPP. Conversely, we observed that mice injected with the cannabinoid CP-55,940 spent significantly more time in the chamber that was paired with the vehicle, suggesting that CP-55,940 may actually induce some aversion, consistent with previous studies in a similar dose range<sup>46</sup>.

## Discussion

From a vast library of virtual molecules, structure-based discovery has led to new agonists that not only potently activate CB1R but are also strongly analgesic without key liabilities of classic cannabinoids. Three observations merit emphasis. **First**, from a tangible library of previously unsynthesized, new to the planet molecules, structure-based docking found new chemotypes for the CB1 receptor, physically distinct from previously known ligands. Using structural complementarity, and the wide range of analogs afforded by the new libraries, we optimized these new ligands, leading to a 1.9 nM K<sub>i</sub> full agonist of the CB1R. **Second**, the pose adopted by active enantiomer of **'3234** (**'1066** / **R-'3234**) in a cryo-EM structure of its complex with CB1R-G<sub>i</sub> superposed closely on the docking prediction, explaining the SAR at atomic resolution and supporting future optimization. **Third**, while the new agonist is strongly anti-allodynic and analgesic across a panel of nociception behavioral assays, **'3234** lacks some of the characteristic adverse drug reactions of most cannabinoid analgesics, with a 10-fold window between analgesia and sedation, and no apparent catalepsy, conditioned place preference or aversion. These traits are unusual for cannabinoids, where sedation often closely tracks with analgesia and where catalepsy is among the “tetrad” of side-effects characteristic of cannabinoid agonists. Encouragingly, combinations of low doses of **'3234** and morphine show improved analgesia, suggesting potential for cotreatments to expand the therapeutic window of each compound on their own.

Three of the four behaviors of the cannabinoid tetrad: hypolocomotion, hypothermia, and catalepsy, are adverse reactions that limit therapeutic potential of the

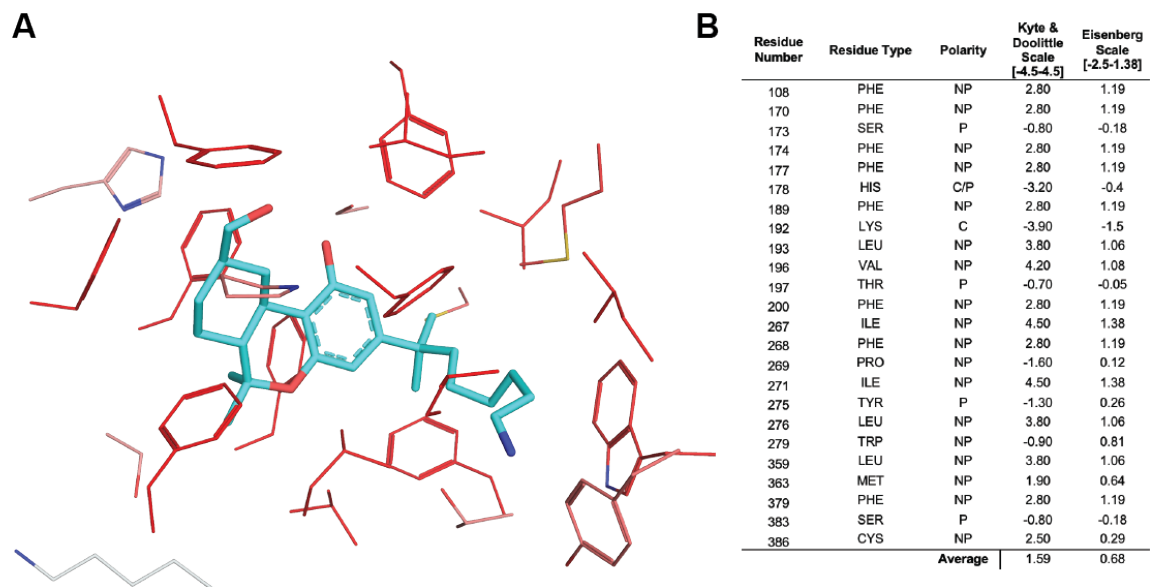
fourth, analgesia. Our hope was that by exploring new chemotypes—afforded by the structure-based approach—some of these adverse aspects of the cannabinoid tetrad could be reduced. This turned out to be the case. While **‘3234** does show some evidence for hypolocomotion, the molecule is substantially less sedating at analgesic doses than is the typical cannabinoid, CP-55,940. We also did not observe catalepsy, even at the highest analgesic dose of **‘3234** tested, whereas CP-55,940 was cataleptic at the same dose. The new agonist induced neither conditioned-place preference nor avoidance at the highest analgesic dose, in contrast to many cannabinoids and to CP-55,940, to which it was compared in this study (**Extended Data Fig. 10J**). These results suggest that major adverse features of cannabinoids can be reduced, perhaps eliminated, without sacrificing analgesia, at least in mouse models.

Several caveats bear mentioning. The mechanistic bases for the disentanglement of sedation and catalepsy from analgesia remains uncertain. Often, clear differences in functional or subtype selectivity (“ligand bias”) support phenotypic differences of different ligands<sup>26,27,38,47</sup>. Here, functional differences between **‘3234**, which does not show some characteristic “tetrad” behaviors, and CP-55,940, which does, were modest, though there were differential functional effects between the CB1 and CB2 subtypes. At this point we can only lay the differences at the door of the new chemotypes explored. Although the initial ligands discovered against CB1R in the docking were at the far low end of the size and hydrophobicity distribution characteristic of cannabinoids, it must be admitted that both terms increased on optimization. Whereas **‘3234** remains smaller and more polar than many potent cannabinoids, the distinction has diminished, as is common during

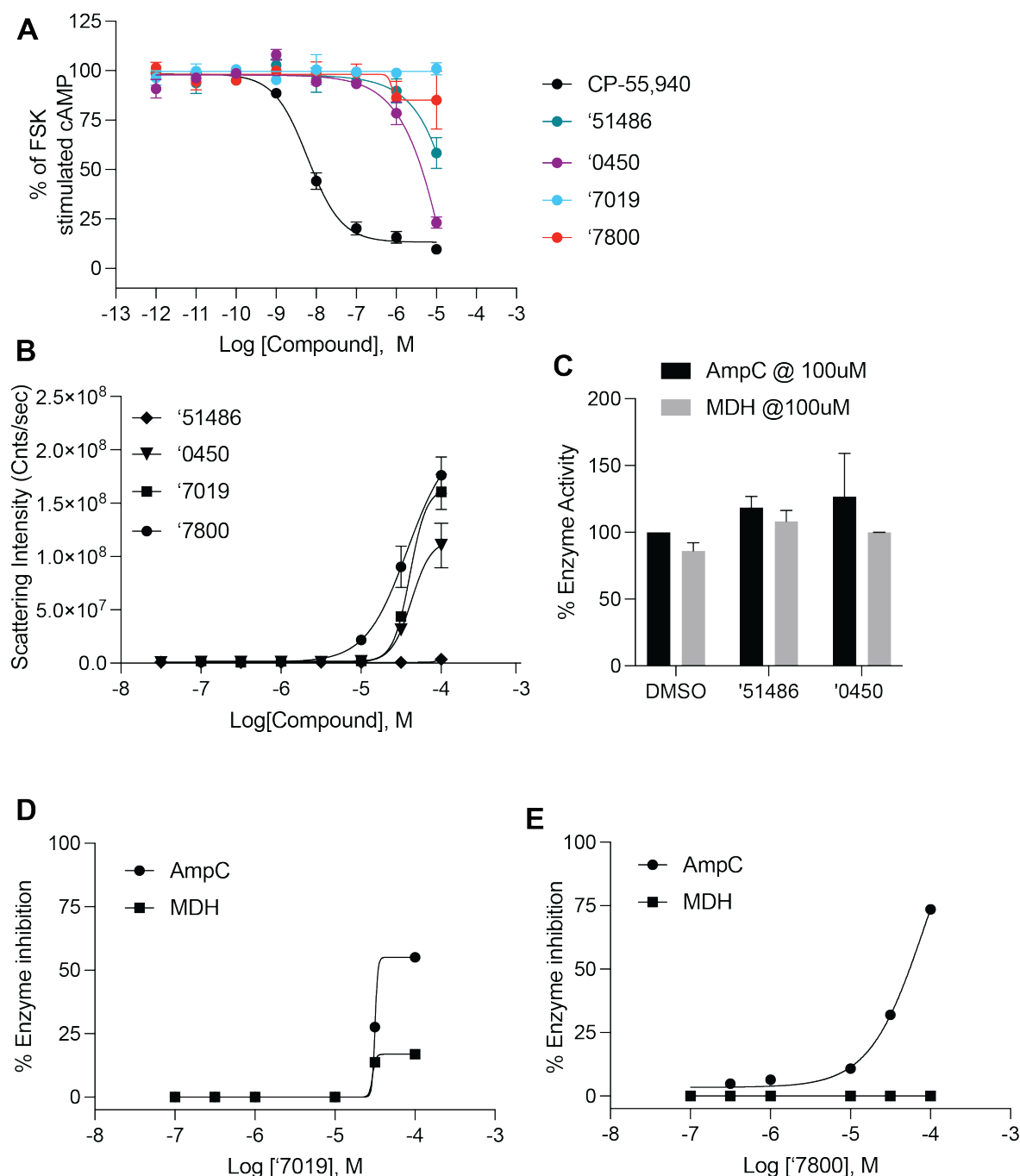
small-molecule hit-to-lead optimization<sup>48</sup>. Still, the ability to find relatively small and polar agonists from the large libraries does hint at the ability to find CB1R ligands in this physical property region. Finally, while the ability to reduce morphine levels to sub-threshold doses by combination with '**3234** is encouraging, the mechanistic basis for this effect, too, is uncertain. Given the crucial role that opioids continue to play in chronic as well as acute pain management, and their dose-limiting side effects and dependence liabilities, addressing the mechanisms that underlie potential additive or synergistic effects of the novel cannabinoids and opioids merits further research.

Despite these caveats, the main observations of this study should be clear. Docking a library of virtual molecules against CB1 revealed new agonist chemotypes, the most promising of which was optimized to the potent full-agonist '**3234**. A cryo-EM structure of the ***R***-'**3234**-CB1-G<sub>i1</sub> complex confirmed its docking-predicted pose. The new agonist was strongly analgesic, and unlike most cannabinoids had a 10-fold therapeutic window over sedation and led to no observable induction of catalepsy. We suspect that there are still further new chemotypes to be discovered that can separate the dose-limiting side-effect aspects of the cannabinoid tetrad while maintaining analgesic potency, supporting the development of new cannabinoid medicines to treat pain.

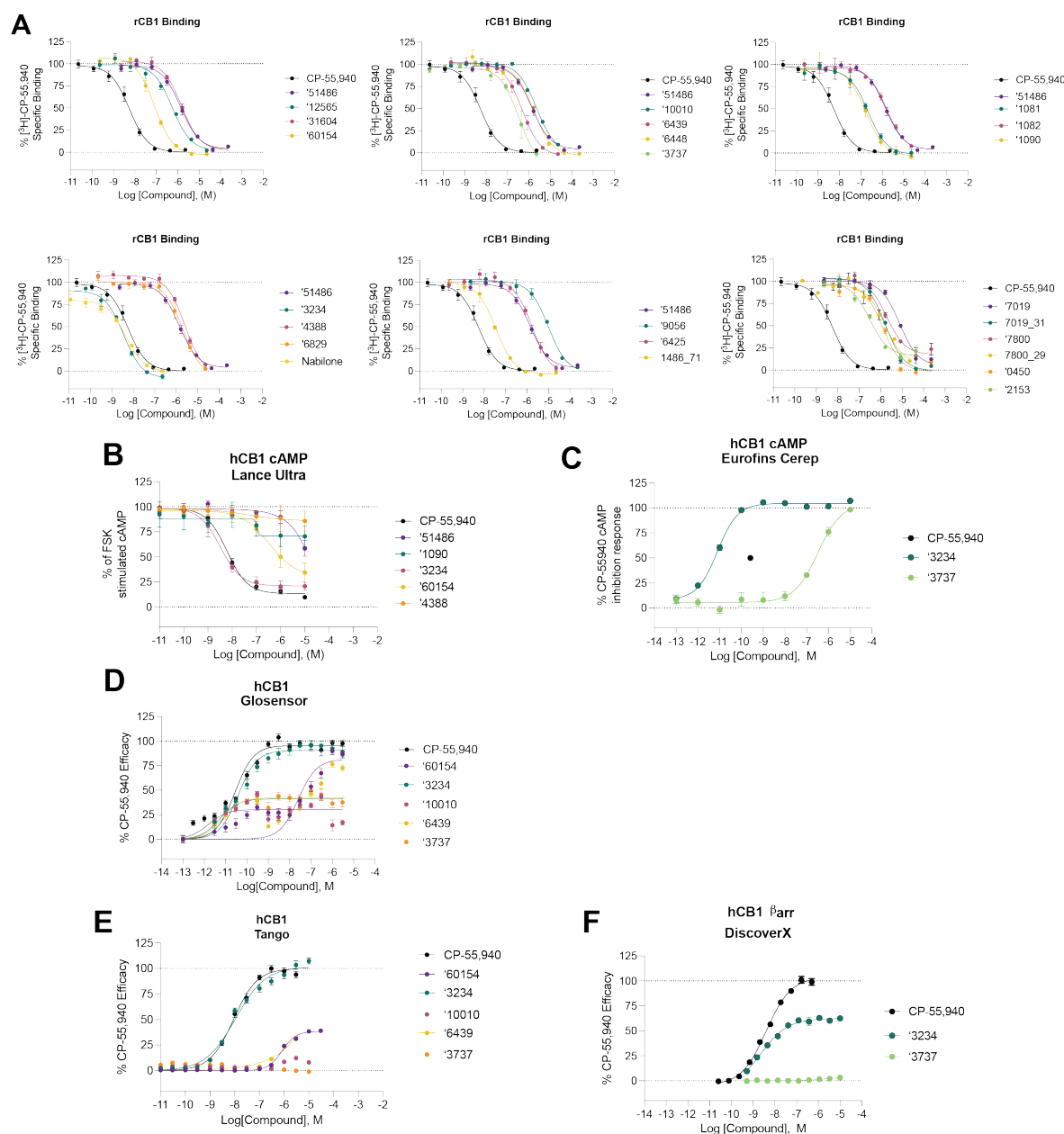
## Extended Data Figures



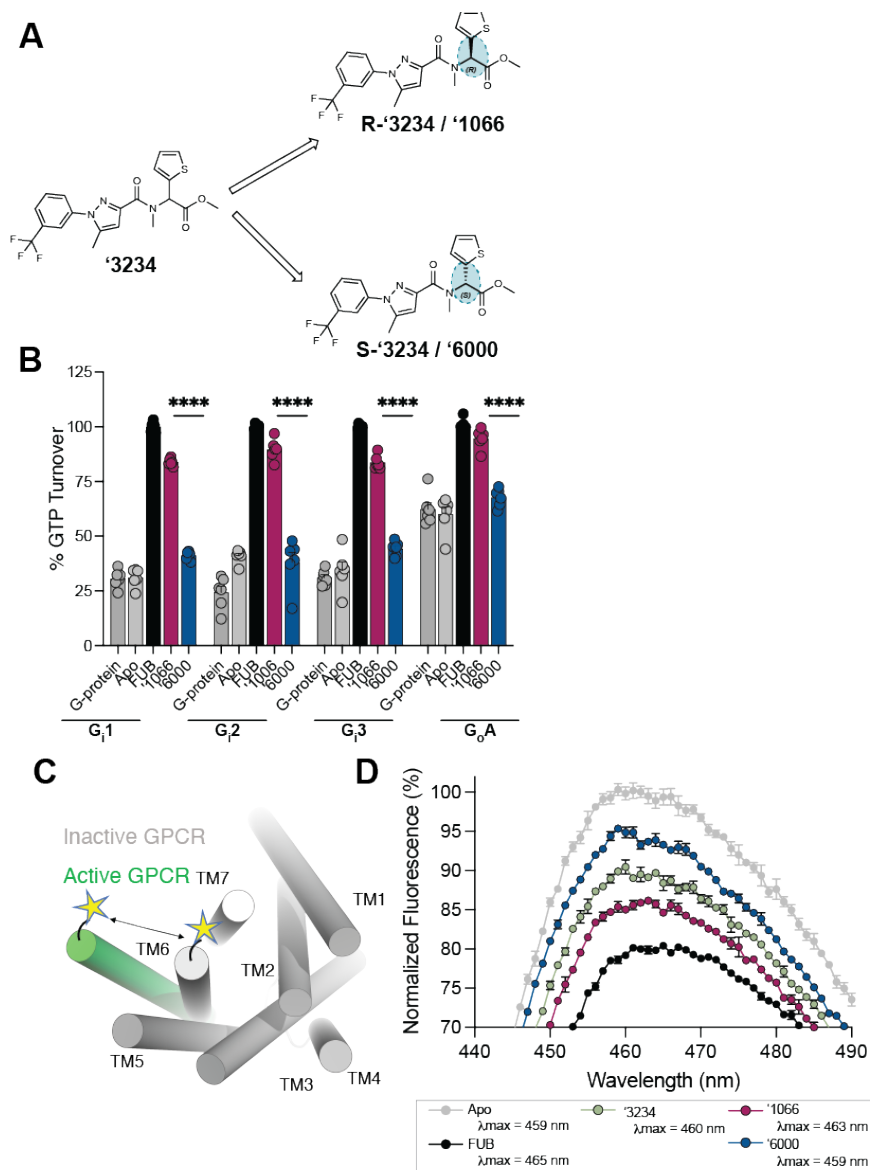
**Extended Data Figure 1.** Hydrophobicity calculations for the hCB1R orthosteric pocket based on PDB: 5XR8. Residues within 5 Å of AM841 are considered. **A.** Depiction of the hCB1 orthosteric pocket, colored by the Eisenberg Scale, where darker red colors indicate more hydrophobic residues and lighter red or gray colors indicate less hydrophobic residues. **B.** A table of the residues within 5 Å of AM841, with their polarity class, and two hydrophobicity scores indicated



**Extended Data Figure 2.** Functional measurements for a subset of screening hits. **A.** Functional cAMP inhibition at hCB1R by the four most potent docking hits. **B.** Scattering intensity in dynamic light scattering experiments of colloidal aggregation. **C.** Inhibition of the off-target enzymes MDH and AmpC Beta-lactamase at 100 uM. **D.** and **E.** Single-point inhibition of the off-target enzymes MDH and AmpC Beta-lactamase by '7019 (**D.**) and '7800 (**E.**). All data represent mean  $\pm$  SEM of three independent experiments in triplicate except **B.** which represents one independent experiment in triplicate.

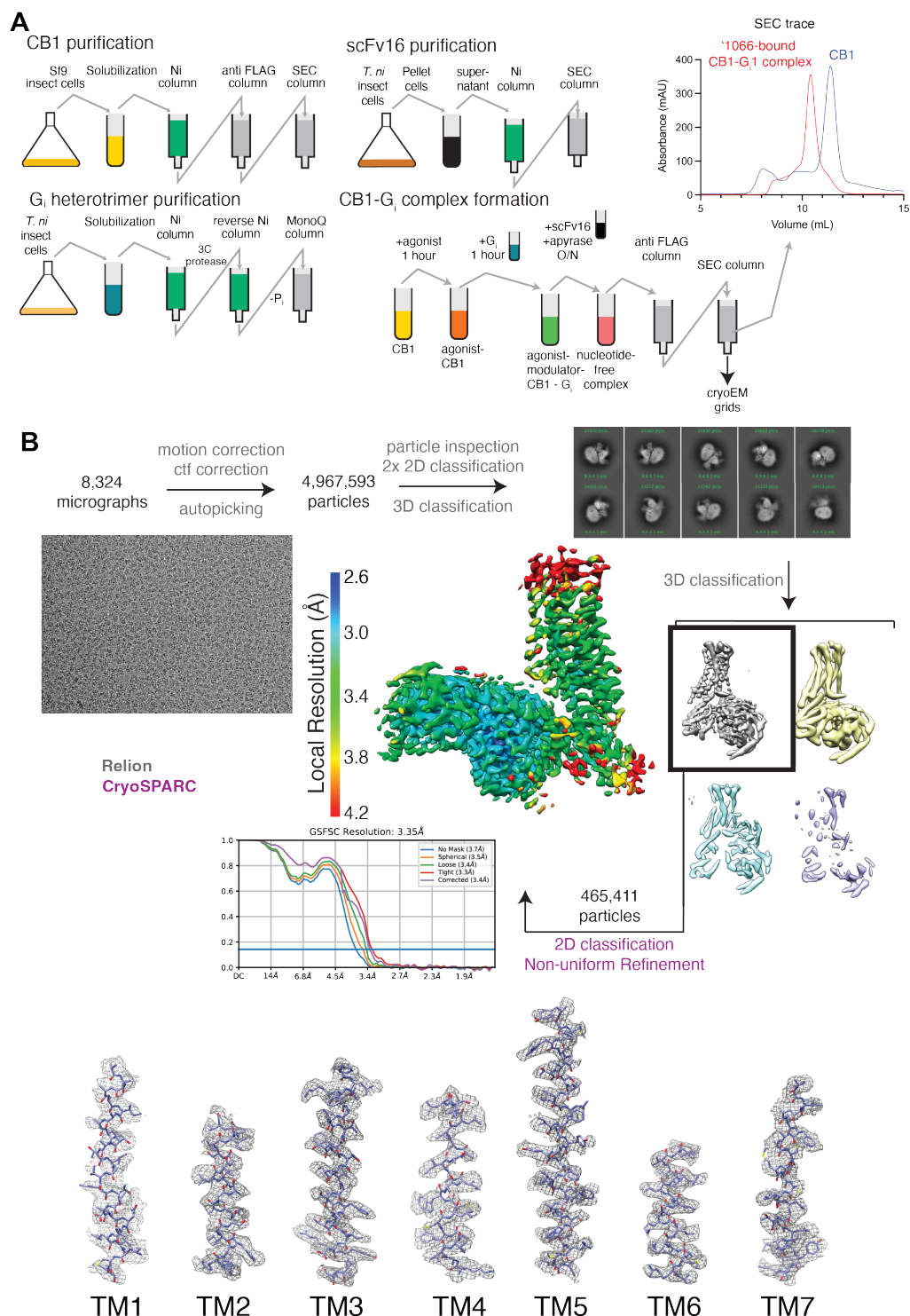


**Extended Data Figure 3.** hCB1 binding and functional data for analogs. **A.** Competition binding data for primary hits and a subset of their analogs at hCB1. **B-D.** Functional cAMP inhibition for a subset of analogs at hCB1 across three separate assays. **E-F.** Functional  $\beta_{arr}$  recruitment for a subset of analogs. All data represent mean  $\pm$  SEM of at least three independent experiments in triplicate except **C.** and **F.** which represent one independent experiment in triplicate. Best fit values can be found in **Supplementary Table 2.**

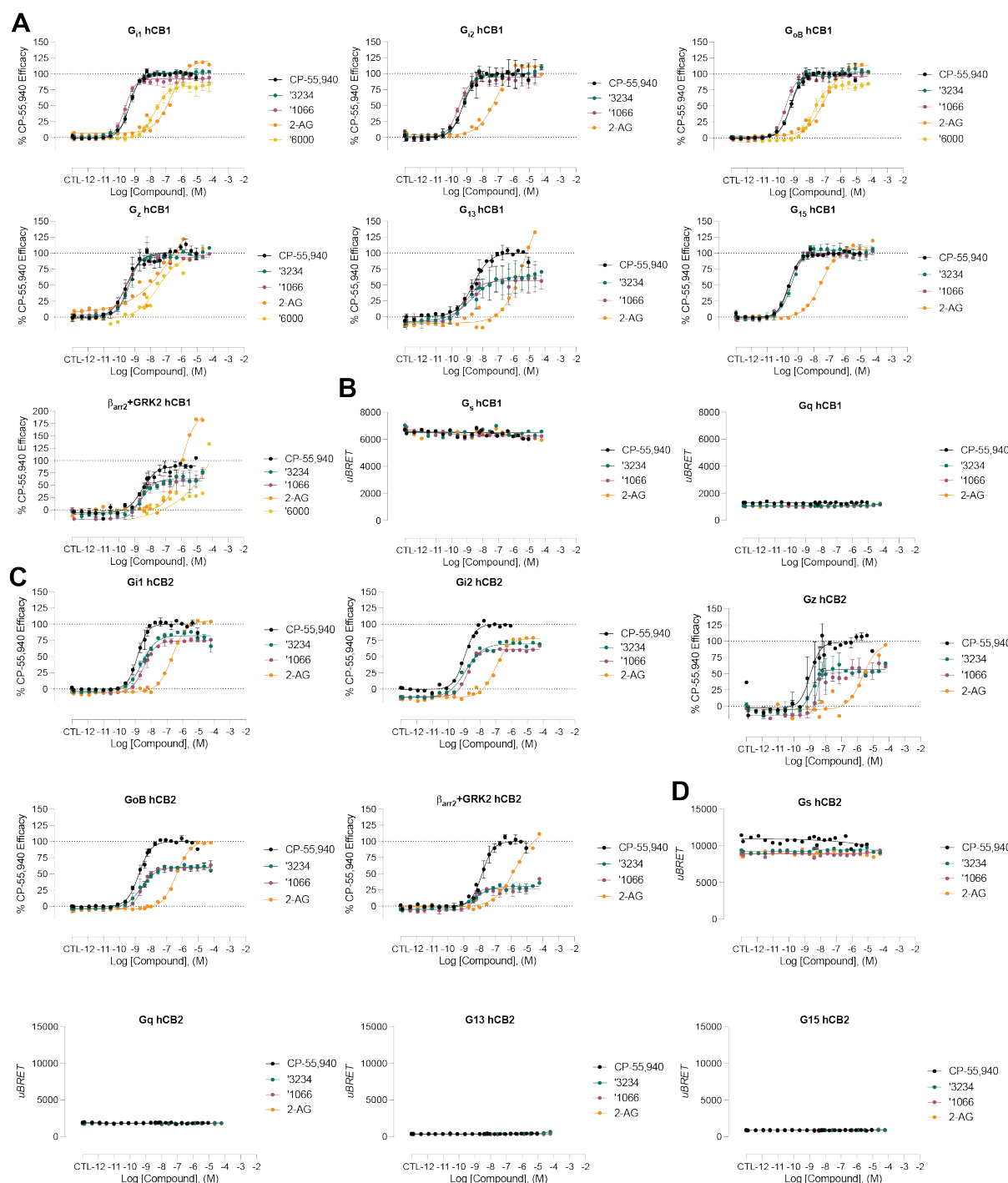


**Extended Data Figure 4.** Additional pharmacological characterization of '3234 and its enantiomers. **A.** Chiral column purification led to the separation of two independent enantiomers, '1066 and '6000. '1066 was determined to be *R*-'3234 from the Cryo-EM structure. **B.** GTPase Glo assay characterizing GTP turnover of G-proteins  $G_{i1-3/o}$ . **C.** Schematic of the environmentally sensitive fluorophore Monobromobimane (Bimane) which when site-specifically labeled (e.g. on TM6) acts as a conformational reporter. **D.** Compared to the apo (grey), the spectrum of full agonist MDMB-fubinaca (Fub)-bound CB1 (black) shows a decrease in intensity and a blue-shift in  $\lambda_{max}$  (Apo 459 nm to Fub 465 nm). The bimane spectrum of '6000 ( $\lambda_{max}$  459 nm, blue) is more similar to apo and the spectrum of '1066 ( $\lambda_{max}$  463 nm, magenta) is closer to that of Fub. The spectrum of the racemate, '3234 (green) is between '1066 (*R*-'3234) and '6000 (*S*-'3234). All data represent mean  $\pm$  SEM of three independent experiments in triplicate.

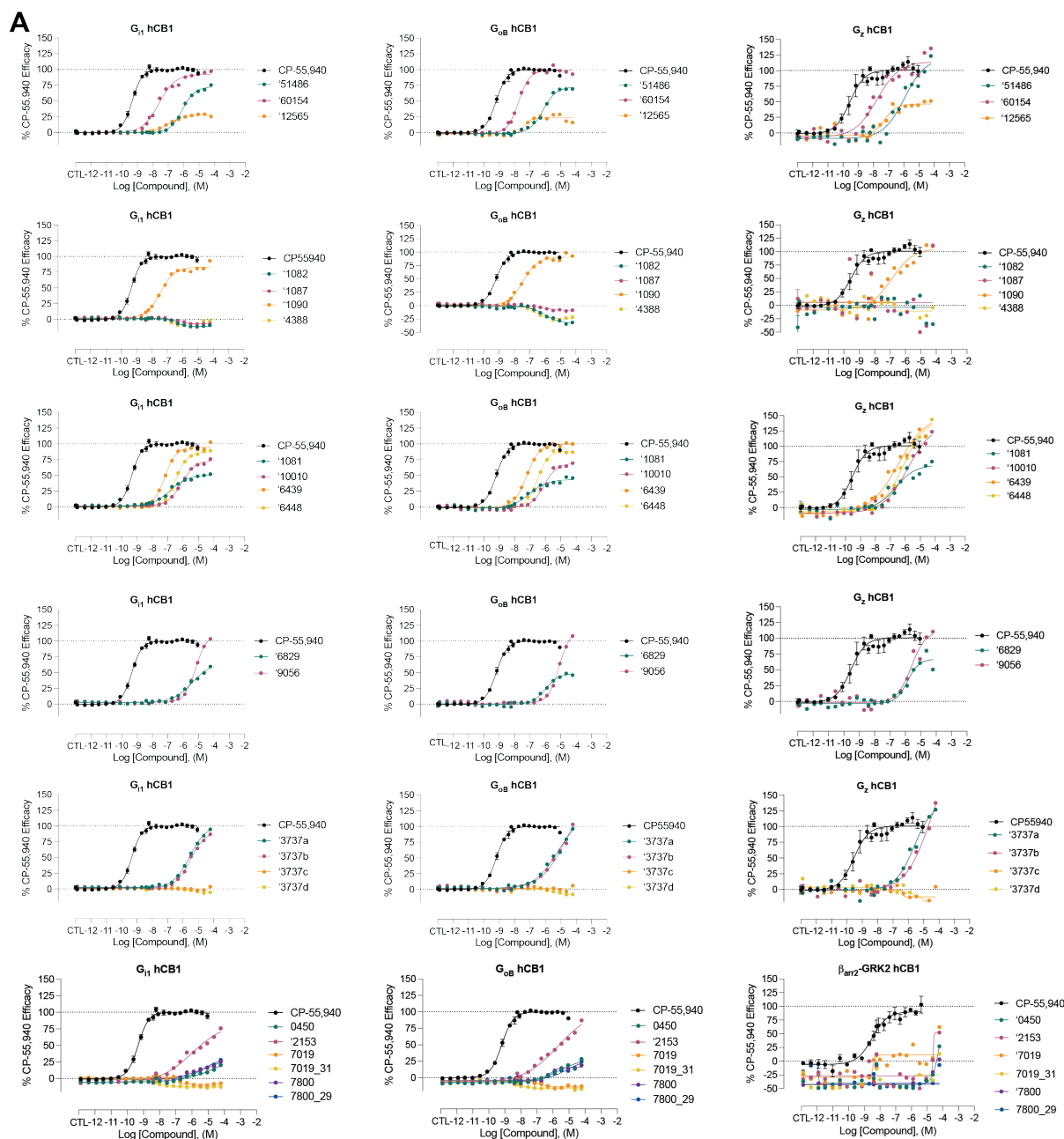




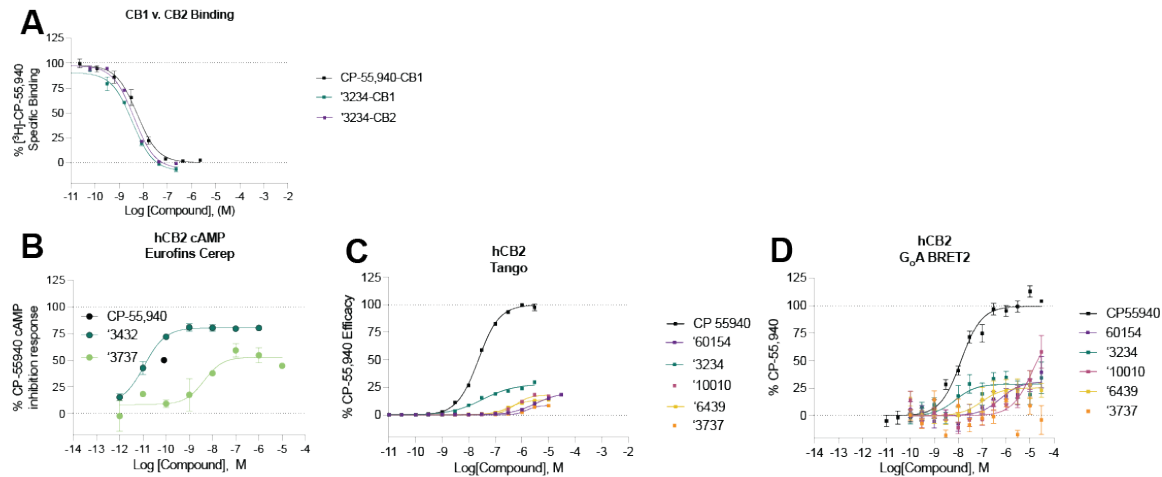
**Extended Data Figure 5. Cryo-EM sample preparation and data processing. A.** Purification of hCB1, scFv16, the G<sub>i</sub> heterotrimer, and complex formation protocols. **B.** Cryo-EM data processing flow chart of CB1, including particle selection, classifications, and density map reconstruction. Details can be found in **Supplementary Table 3**.



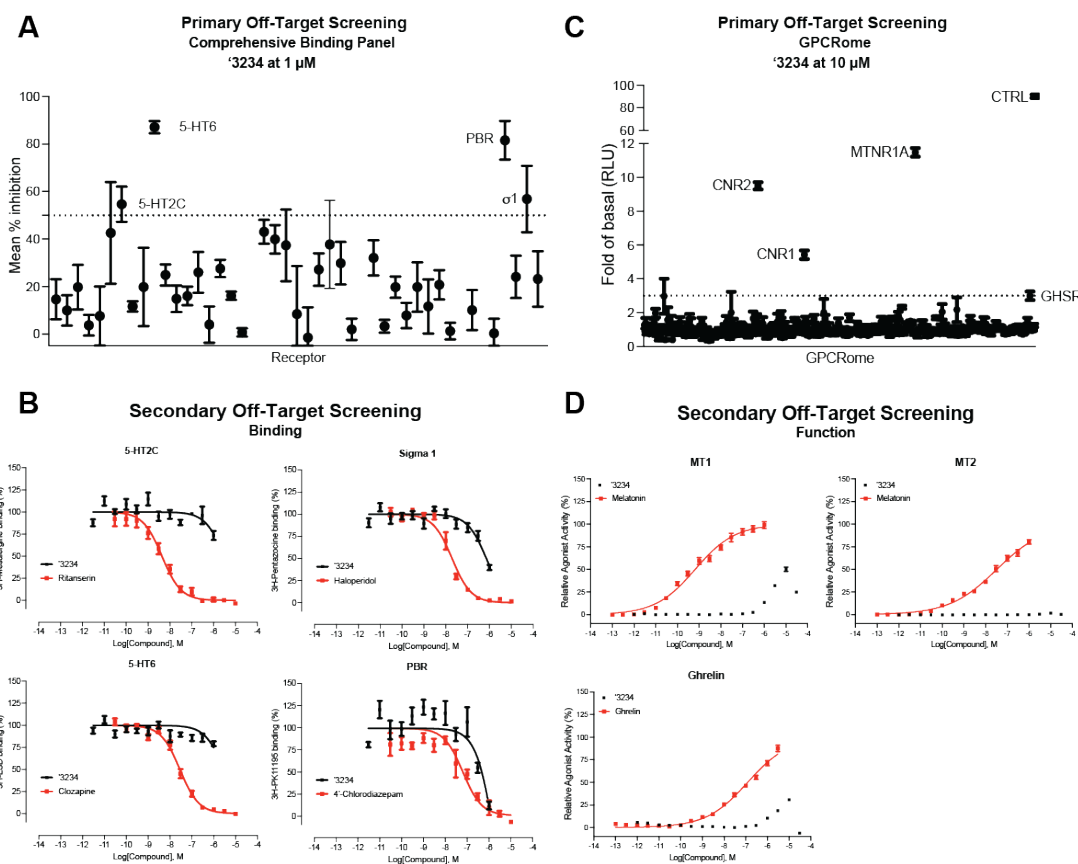
**Extended Data Figure 6.** hCB1/2 functional data for select analogs in the bioSens-All® platform. **A.** Normalized activity for select analogs versus a panel of sensors in hCB1-expressing cells. **B.** Raw BRET activity for select analogs versus  $G_s$  and  $G_q$  in hCB1-expressing cells. **C.** Normalized activity for select analogs versus a panel of sensors in hCB2-expressing cells. **D.** Raw BRET activity for select analogs versus  $G_s$ ,  $G_q$ ,  $G_{12}$ , and  $G_{15}$  in hCB2-expressing cells. Best fit values and experimental replicate counts can be found in **Supplementary Table 5 & 8.**



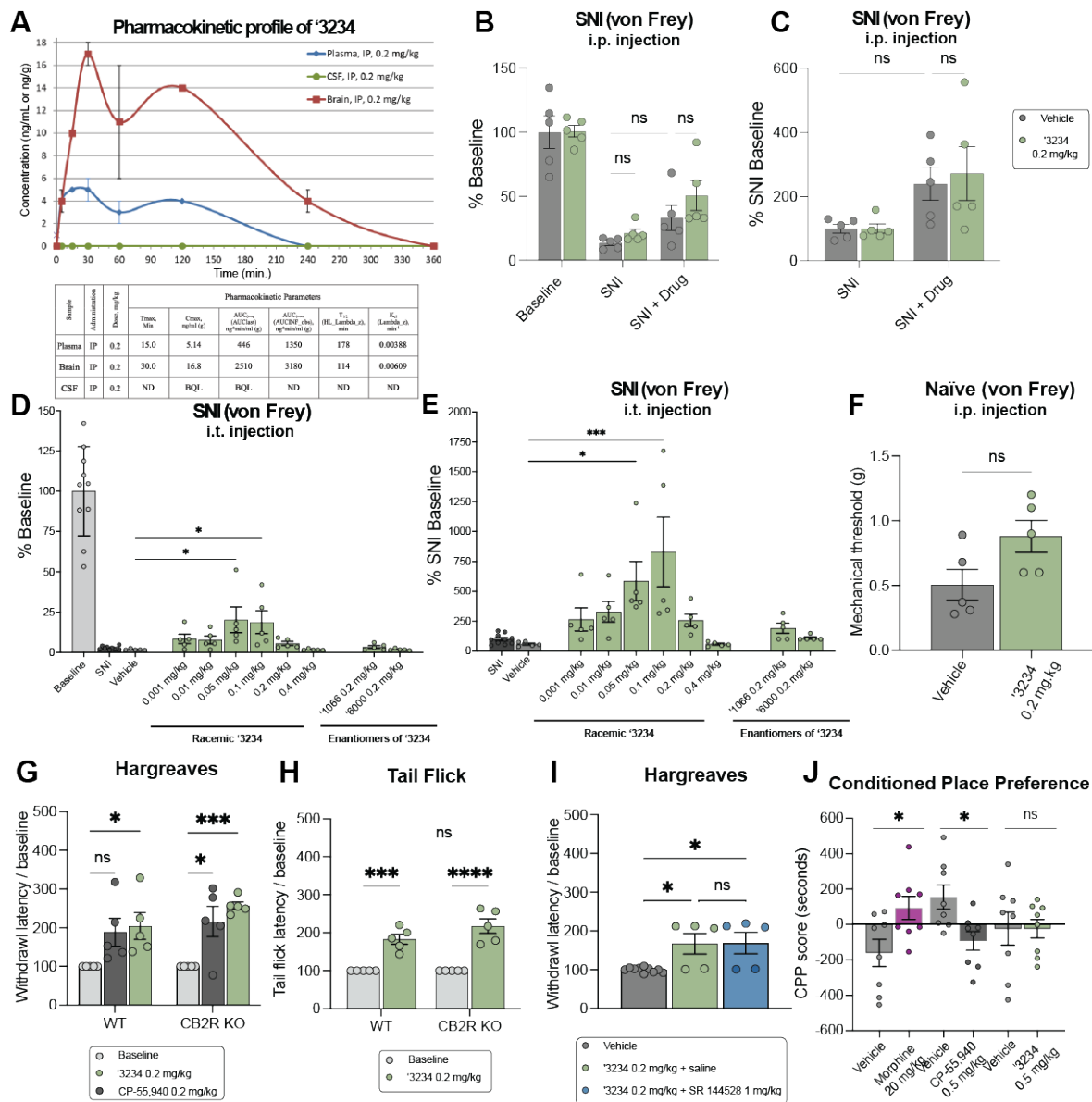
**Extended Data Figure 7.** hCB1 functional data for select analogs in the bioSens-All® platform. **A.** Normalized activity for select analogs versus a panel of sensors in hCB1-expressing cells. Best fit values and experimental replicate counts can be found in **Supplementary Table 4**.



**Extended Data Figure 8.** CB2 binding and functional data for select analogs. **A.** Competition binding data shows that '3234 is equipotent at CB1 and CB2 (rCB1 pKi = 8.7 (95% CI 8.60 – 8.86), hCB2 pKi = 8.6 (95% CI 8.55 – 8.77);  $t(4) = 5.13$ ,  $p = 0.007$ ). **B-D.** Functional cAMP inhibition for a subset of analogs at hCB2 across three separate assays. All data represent mean  $\pm$  SEM of three independent experiments in triplicate except **B.** which represents one independent experiment in triplicate. Best fit values can be found in **Supplementary Table 7.**



**Extended Data Figure 9.** Off-target profiling of '3234. **A.** Comprehensive binding data against a panel of 45 common GPCR and non-GPCR drug targets. **B.** Follow-up dose response binding experiments for targets with > 50% inhibition in the single-point experiments. **C.** TANGO screens against a panel of 320 GPCRs for '3234. **D.** Follow-up dose response functional experiments for targets with > 3-fold activation in the single-point experiments. Data in **A.**, **C.**, and **D.** represent mean  $\pm$  SEM of 3 independent experiments in triplicate. Data in **B.** represent mean  $\pm$  SEM of 2 independent experiments in triplicate except 5-HT6 which is 3 independent experiments in triplicate.





**Extended Data Figure 10.** Pharmacokinetic, analgesic, side-effect, and permeability profile of ‘3234. **A.** Pharmacokinetic profile of ‘3234 after a single 0.2 mg/kg dose in brain, CSF, and plasma compartments. Data represent mean  $\pm$  SEM of 3 animals per timepoint. **B.** Effect of ‘3234 (i.p.) in neuropathic pain model in mice after SNI with mechanical allodynia ( $n = 5$ ; two-way ANOVA; SNI x drug treatment interaction:  $F(2, 24) = 0.5$ ,  $P > 0.05$ ; SNI:  $F(2, 24) = 51.8$ ,  $P < 0.0001$ ; drug treatment:  $F(1, 24) = 1.6$ ,  $P > 0.05$ ; asterisks define individual group differences to vehicle control after Tukey’s multiple comparisons post-hoc test correction). Data presented are normalized to pre-SNI baseline measurements. **C.** Effect of ‘3234 (i.p.) in neuropathic pain model in mice after SNI with mechanical allodynia ( $n = 5$ ; two-way ANOVA; SNI x drug treatment interaction:  $F(1, 16) = 0.1$ ,  $P > 0.05$ ; SNI:  $F(1, 16) = 9.6$ ,  $P = 0.007$ ; drug treatment:  $F(1, 16) = 0.1$ ,  $P > 0.05$ ; asterisks define individual group differences to vehicle control after Tukey’s multiple comparisons post-hoc test correction). Data presented are normalized to post-SNI baseline measurements. **D.** Effect of ‘3234 (i.t.) in neuropathic pain model in mice after SNI with mechanical allodynia ( $n = 5$ ; one-way ANOVA,  $F(6, 28) = 4.2$ ,  $P = 0.004$ ; asterisks define individual group differences to vehicle control after Dunnett’s multiple comparisons post-hoc test correction). Data presented are normalized to pre-SNI baseline measurements. **E.** Effect of ‘3234 (i.t.) in neuropathic pain model in mice after SNI with mechanical allodynia ( $n = 5$ ; one-way ANOVA,  $F(7, 32) = 3.8$ ,  $P = 0.004$ ; asterisks define individual group differences to vehicle control after Dunnett’s multiple comparisons post-hoc test correction). Data presented are normalized to post-SNI baseline measurements. **F.** Effect of ‘3234 (i.p.) in naïve (non-SNI) mice in the mechanical assay (all  $n = 5$ ; two-tailed unpaired t-test,  $t(8) = 2.17$ ,  $P > 0.05$ ). **G.** Comparison of the effect of ‘3234 and CP-55,940 in wildtype (WT) versus CB2R knockout (KO) mice in the Hargreaves assay (all  $n = 5$ ; two-way ANOVA; genotype x drug treatment interaction:  $F(2, 24) = 0.5$ ,  $P > 0.05$ ; genotype:  $F(1, 24) = 1.6$ ,  $P > 0.05$ ; drug treatment:  $F(2, 24) = 13.8$ ,  $P = 0.0001$ ; asterisks define individual group differences to baseline after Tukey’s multiple comparisons post-hoc test correction). **H.** Comparison of the effect of ‘3234 in wildtype (WT) versus CB2R knockout (KO) mice in the Tail Flick assay (all  $n = 5$ ; two-way ANOVA; genotype x drug treatment interaction:  $F(1, 16) = 2.2$ ,  $P > 0.05$ ; genotype:  $F(1, 16) = 2.2$ ,  $P > 0.05$ ; drug treatment:  $F(1, 16) = 72.3$ ,  $P < 0.0001$ ; asterisks define individual group differences to baseline after Šídák’s multiple comparisons post-hoc test correction). **I.** Withdrawal latency in the Hargreaves assay after co-treatment with the selective CB2R antagonist SR 144528 (1 mg/kg) (all  $n = 5$ ; one-way ANOVA,  $F(2, 17) = 6.6$ ,  $P = 0.008$ ; asterisks define individual group differences to vehicle control after Tukey’s multiple comparisons post-hoc test correction). **J.** Comparison of morphine ( $n = 8$ ; two-tailed unpaired t-test,  $t(14) = 2.51$ ,  $P = 0.03$ ) to CP-55,940 ( $n = 8$ ; two-tailed unpaired t-test,  $t(14) = 2.9$ ,  $P = 0.01$ ) and ‘3234 ( $n = 8$ ; two-tailed unpaired t-test,  $t(14) = 0.005$ ,  $P > 0.05$ ) in the Conditioned Place Preference (CPP) test. For all statistical tests: ns, not significant, \* $P < 0.05$ , \*\* $P < 0.01$ , \*\*\* $P < 0.001$ , \*\*\*\* $P < 0.0001$ . All data represent mean  $\pm$  SEM of 3-10 animals.

## Methods

**Molecular docking.** A crystal structure of the active-state CB1 receptor (PDB: 5XR8)<sup>16</sup> was used for docking calculations. As the goal was to find small-molecule, non-phytocannabinoid ligands, we used ligand coordinates from the cryogenic ligand MDMB-Fubinaca (PDB: 6N4B)<sup>18</sup>, after overlaying the two receptor structures. The coordinates of Met363<sup>6,55</sup> were modified slightly, while maintaining the residue within the electron density to reduce a clash with the overlaid ligand indole group. The combined coordinates were minimized with Schrödinger's Maestro prior to calculation of the docking energy potential grids. These grids were precalculated using CHEMGRID<sup>49</sup> for AMBER<sup>50</sup> van der Waals potential, QNIFFT<sup>51</sup> for Poisson-Boltzmann-based electrostatic potentials, and SOLVMAP<sup>52</sup> for context-dependent ligand desolvation. Atoms of the ligand determined in the cryo-EM structure (PDB: 6N4B), MDMB-Fubinaca, were used to seed the matching sphere calculation in the orthosteric site, with 45 total spheres used (these spheres act as pseudo-atoms defining favorable sub-sites on to which library molecules may be superposed<sup>53</sup>). The receptor structure was protonated using REDUCE<sup>54</sup> and AMBER united atom charges were assigned<sup>50</sup>. Control calculations<sup>55</sup> using 324 known ligands extracted from the IUPHAR database<sup>56</sup>, ChEMBL24<sup>32</sup>, and ZINC15, and 14,929 property-matched decoys<sup>57</sup> were used to optimize docking parameters based on enrichment measured by logAUC<sup>55</sup>, prioritization of neutral over charged molecules, and by the reproduction of expected and known binding modes of CB<sub>1</sub> ligands. SPHGEN<sup>53</sup> was used to generate pseudo-atoms to define the extended low protein dielectric and desolvation region<sup>22,58</sup>. The protein low dielectric and desolvation regions were extended as previously described<sup>59</sup>, based on control calculations, by a radius of 1.5 Å and 1.9 Å,



respectively. The desolvation volume was removed around S383<sup>7,39</sup> and H178<sup>2,65</sup> to decrease the desolvation penalty near these residues and to increase the number of molecules that would form polar contacts with them.

A subset of 74 million large, relatively hydrophobic molecules from the ZINC15 database (<http://zinc15.docking.org>), with calculated octanol-water partition coefficients (cLogP, calculated using JChem-15.11.23.0, ChemAxon; <https://www.chemaxon.com>) between  $3 \leq 5$  and with molecular mass from 350 Da to  $\geq 500$  Da, was docked against the CB<sub>1</sub> orthosteric site using DOCK3.7<sup>60</sup>. Of these, more than 18 million successfully fit. An average of 4,706 orientations, and for each orientation, an average of 645 conformations was sampled. Overall, about 64 trillion complexes were sampled and scored. The total time was about 25,432 core hours, or less than 18 wall-clock hours on 1,500 cores.

To reduce redundancy of the top scoring docked molecules, the top 300,000 ranked molecules were clustered by ECFP4-based Tanimoto coefficient (Tc) of 0.5, and the best scoring member was chosen as the cluster representative molecule. These 60,420 clusters were filtered for novelty by calculating the Tc against >7,000 CB<sub>1</sub> and CB<sub>2</sub> receptor ligands from the ChEMBL24<sup>32</sup> database. Molecules with  $Tc \geq 0.38$  to known CB<sub>1</sub>R/CB<sub>2</sub>R ligands were not pursued further.

After filtering for novelty, the docked poses of the best-scoring members of each cluster were filtered by the proximity of their polar moieties to Ser383<sup>7,39</sup>, Thr201<sup>3,37</sup>, or

His178<sup>2,65</sup>, and visually inspected for favorable geometry and interactions. For the most favorable molecules, all members of its cluster were also inspected, and one of these was chosen to replace the cluster representative if they exhibited more favorable poses or chemical properties. Ultimately, 60 compounds were chosen for synthesis and testing.

**Make-on-demand synthesis and purity information.** Of these 60, 52 were successfully synthesized by Enamine (an 87% fulfilment), but only 46 were ultimately screened due to poor DMSO solubility of six of the ordered ligands. The purities of active molecules and analogs synthesized by Enamine were at least 90% and typically above 95%. For bespoke compound synthesized in house purities were at least 95% and typically above 98%. The purity of compounds tested *in vivo* were >95% and typically above 98%. Synthetic routes<sup>61</sup>, chemical characterization, and purity quality control information for a subset of hits can be found in the supplementary information file.

**Ligand optimization.** Analogs with ECFP4 Tcs  $\geq 0.5$  to the four most potent docking hits ('51486, '0450, '7800, and '7019) were queried in Arthor and SmallWorld (<https://sw.docking.org>, <https://arthor.docking.org>; NextMove Software, Cambridge UK) against 1.4 and 12 Billion tangible libraries, respectively, the latter primarily containing Enamine REAL Space compounds (<https://enamine.net/compound-collections/real-compounds/real-space-navigator>). Results were pooled, docked into the CB1R site, and filtered using the same criteria as the original screen. Between 11 and 30 analogs were synthesized for each of the four scaffolds. Second- and third-round analogs were

designed in 2D space based on specific hypotheses and were synthesized at Enamine or at Northeastern University.

**Radioligand Binding Experiments.** The binding affinities of the compounds were obtained by competition binding using membrane preparations from rat brain (source of CB1) or HEK293 cells stably expressing human CB2 receptors and [<sup>3</sup>H]-CP-55,940 as the radioligand, as described<sup>62</sup>. The results were analyzed using nonlinear regression to determine the IC<sub>50</sub> and K<sub>i</sub> values for each ligand (Prism by GraphPad Software, Inc., San Diego, CA). The K<sub>i</sub> values are expressed as the mean of two to three experiments each performed in triplicate.

## Functional assays

**Lance Ultra cAMP Accumulation Assay.** The inhibition of forskolin-stimulated cAMP accumulation assays was carried out using PerkinElmer's Lance Ultra cAMP kit following the manufacturer's protocol. In brief, CHO cells stably expressing human CB1 were harvested by incubation with Versene (ThermoFisher Scientific, Waltham, MA) for 10 min, washed once with Hank's Balanced Salt Solution, and resuspended in stimulation buffer at ~200 cells/μL density. The ligands at eight different concentrations (0.001-10,000 nM) in stimulation buffer (5 μL) containing forskolin (2 μM final concentration) were added to a 384-well plate followed by the cell suspension (5 μL; ~1000 cells/well). The plate was incubated for 30 min at room temperature. Eu-cAMP tracer (5 μL) and Ulight-anti-cAMP (5 μL) working solutions were then added to each well, and the plate was incubated at room temperature for an additional 60 min. Results were measured on a

Perkin-Elmer EnVision plate reader. The EC<sub>50</sub> values were determined by nonlinear regression analysis using Prism software (GraphPad Software, Inc., San Diego, CA) and are expressed as the mean of three experiments, each performed in triplicate.

**Cerep cAMP Inhibition Assay.** Compounds ‘3234 and ‘3737 were run through the Cerep HTRF cAMP assay for functional activity as agonists (catalog number 1744; Cerep, Eurofins Discovery Services; France). The hCB1 CHO-K1 cells are suspended in HBSS buffer (Invitrogen) complemented with 20 mM HEPES (pH 7.4), then distributed in microplates at a density of 5.103 cells/well in the presence of either of the following: HBSS (basal control), the reference agonist at 30 nM (stimulated control) or the test compounds. Thereafter, the adenylyl cyclase activator forskolin is added at a final concentration of 25 µM. Following 30 min incubation at 37°C, the cells are lysed, and the fluorescence acceptor (D2-labeled cAMP) and fluorescence donor (anti-cAMP antibody labeled with europium cryptate) are added. After 60 min at room temperature, the fluorescence transfer is measured at  $\lambda_{ex}$ =337 nm and  $\lambda_{em}$ =620 and 665 nm using a microplate reader (Envision, Perkin Elmer). The cAMP concentration is determined by dividing the signal measured at 665 nm by that measured at 620 nm (ratio). The results are expressed as a percent of the control response to 10 nM CP-55,940. Each measurement was done in triplicate.

**GloSensor cAMP Accumulation Assay.** The GloSensor cAMP accumulation assay was performed as secondary validation assays (dose-response setup) as described in detail on the NIMH PDSP website at

<https://pdsp.unc.edu/pdspweb/content/PDSP%20Protocols%20II%202013-03-28.pdf>.

The results were analysed using GraphPad Prism 9. Each experiment was performed in triplicate and functional IC<sub>50</sub> values were determined from the mean of three independent experiments.

**TRUPATH BRET2 G<sub>oA</sub> recruitment for CB2R.** CB2 receptor was co-expressed with. G<sub>oA</sub> dissociation BRET2 assays were performed as previously described with minor modifications<sup>63</sup>. In brief, HEK293T cells were co-transfected overnight with human CB2 receptor, G<sub>αo</sub>A-RLuc, G<sub>β3</sub>, and G<sub>γ9</sub>-GFP2 constructs. After 18–24 hours, the transfected cells were seeded into poly-L-lysine-coated 384-well white clear-bottom cell culture plates at a density of 15,000–20,000 cells and incubated with DMEM containing 1% dialyzed FBS, 100 U mL<sup>-1</sup> of penicillin and 100 µg mL<sup>-1</sup> of streptomycin for another 24 hours. The next day, the medium was aspirated and washed once with 20 µL of assay buffer (1× HBSS, 20 mM HEPES, 0.1% BSA, pH 7.4). Then, 20 µL of drug buffer containing coelenterazine 400a (Nanolight Technology) at 5 µM final concentration was added to each well and incubated for 5 minutes, followed by the addition of 10 µL of 3X designated drug buffer for 5 minutes. Then, 10 µL of 4X final concentrations of ligands were added for 5 minutes. Finally, the plates were read in PHERAstar FSX (BMG Labtech) with a 410-nm (RLuc8-coelenterazine 400a) and a 515-nm (GFP2) emission filter, at 0.6-second integration times. BRET ratio was computed as the ratio of the GFP2 emission to RLuc8 emission. Data were normalized to percentage of CP-55,940 and analyzed in GraphPad Prism 9.1. Each experiment was performed in triplicate and functional IC<sub>50</sub> values were determined from the mean of four independent experiments.

**Tango  $\beta$ -Arrestin-2 Recruitment Assay.** The Tango  $\beta$ -Arrestin-2 recruitment assays were performed as described<sup>64</sup>. In brief, HTLA cells were transiently transfected with human CB1 or CB2 Tango DNA construct overnight in DMEM supplemented with 10 % FBS, 100  $\mu\text{g ml}^{-1}$  streptomycin and 100 U  $\text{ml}^{-1}$  penicillin. The transfected cells were then plated into poly-L-lysine-coated 384-well white clear-bottom cell culture plates in DMEM containing 1% dialysed FBS at a density of 10,000–15,000 cells per well. After incubation for 6 h, the plates were added with drug solutions prepared in DMEM containing 1% dialysed FBS for overnight incubation. On the day of assay, medium and drug solutions were removed and 20  $\mu\text{l}$  per well of BrightGlo reagent (Promega) was added. The plates were further incubated for 20 min at room temperature and counted using the Wallac TriLux Microbeta counter (PerkinElmer). The results were analysed using GraphPad Prism 9. Each experiment was performed in triplicate and functional  $\text{IC}_{50}$  values were determined from the mean of three independent experiments.

**DiscoverX PathHunter<sup>®</sup>  $\beta$ -Arrestin-2 Recruitment Assay.** ‘3234 and ‘3737 were run through the PathHunter<sup>®</sup>  $\beta$ -Arrestin-2 assay (catalog number 86-0001P-2070AG; DiscoverX, Eurofins Discovery Services; CA, USA). PathHunter cell lines (CHO-K1 lineage expressing hCB1) were expanded from freezer stocks according to standard procedures. Cells were seeded in a total volume of 20  $\mu\text{L}$  into white walled, 384-well microplates and incubated at 37°C for the appropriate time prior to testing. For agonist determination, cells were incubated with sample to induce response. Intermediate dilution of sample stocks was performed to generate 5X sample in assay buffer. 5  $\mu\text{L}$  of 5X sample

was added to cells and incubated at 37°C or room temperature for 90 to 180 minutes. Vehicle concentration was 1%. Assay signal was generated through a single addition of 12.5 or 15 µL (50% v/v) of PathHunter Detection reagent cocktail, followed by a 1-hour incubation at room temperature. Microplates were read following signal generation with a PerkinElmer Envision™ instrument for chemiluminescent signal detection. Compound activity was analyzed using CBIS data analysis suite (ChemInnovation, CA). Percentage activity was calculated using the following equation:

$$\% \text{ CP-55,940 activity} = 100 \times \frac{(\text{mean RLU}_{\text{test sample}} - \text{mean RLU}_{\text{vehicle}})}{(\text{mean max}_{\text{CP-55,940}} - \text{mean RLU}_{\text{CP-55,940}})}$$

The data were analyzed in GraphPad Prism 9.1 using “dose–response–stimulation log(agonist) versus response (four parameters)” and data were presented as EC<sub>50</sub> or pEC<sub>50</sub> ± CIs of one independent experiment in duplicate.

**Signaling profiling of hCB1 and hCB2 using bioSensAll®.** ebBRET-based effector membrane translocation biosensor assays were conducted at Domain Therapeutics NA Inc. (Montreal, QC, Canada) as previously described<sup>39</sup>. CP-55,940, 2-AG and 25 test compounds were assayed for their effect on the signaling signature of the human cannabinoid receptor type 1 or 2 (hCB1 or hCB2) using the following bioSensAll® sensors: the heterotrimeric G protein activation sensors (G<sub>as</sub>, G<sub>ai1</sub>, G<sub>ai2</sub>, G<sub>aoB</sub>, G<sub>az</sub>, G<sub>α13</sub>, G<sub>αq</sub>, G<sub>α15</sub>) and the βarrestin-2 plasma membrane (PM) recruitment sensor (in the presence of GRK2 overexpression). HEK293 cells were maintained in Dulbecco's Modified Eagle Medium (DMEM) (Wisent) supplemented with 1% penicillin- streptomycin (Wisent) and 10% (or 2 % for transfection) fetal bovine serum (Wisent) at 37°C with 5%



CO2. All biosensor-coding plasmids and related information are the property of Domain Therapeutics NA Inc. The total amount of transfected DNA was adjusted and kept constant at 1 µg per mL of cell culture to be transfected using salmon sperm DNA (Invitrogen) as 'carrier' DNA, PEI (polyethylenimine 25 kDa linear, PolyScience) and DNA (3:1 ml PEI:mg DNA ratio) were first diluted separately in 150 mM NaCl then mixed and incubated for at least 20 minutes at room temperature to allow for the formation of DNA/PEI complexes. During the incubation, HEK293 cells were detached, counted, and re-suspended in maintenance medium to a 350,000 cells per mL density. At the end of the incubation period, the DNA/PEI mixture was added to the cells. Cells were finally distributed in 96-well plates (White Opaque 96-well /Microplates, Greiner) at a density of 35,000 cells per well. Forty-eight hours post-transfection, medium was aspirated and replaced with 100 µl of Hank's Balanced Salt Solution buffer (HBSS) (Wisent) per well using 450-Select TS Biotek plate washer. After 60 min incubation in this medium, 10 µL of 10 µM e-Coelenterazine Prolume Purple (Methoxy e-CTZ) (Nanolight) was added to each well for a final concentration of 1 µM immediately followed by addition of increasing concentrations of the test compounds to each well using the HP D300 digital dispenser (Tecan). All compounds were assayed at 22 concentrations with each biosensor after a 10-minute room temperature incubation period. BRET readings were collected with a 0.4 sec integration time on a Synergy NEO plate reader (BioTek Instruments, Inc., USA; filters: 400nm/70nm, 515nm/20nm). BRET signals were determined by calculating the ratio of light emitted by GFP-acceptor (515nm) over light emitted by luciferase-donor (400nm). All BRET ratios were standardized using the universal BRET (uBRET) equation:

$$uBRET = \left( \frac{BRET\ ratio - A}{B - A} \right) \times 10,000$$

where  $A$  is the BRET ratio obtained from transfection of negative control and  $B$  is the BRET ratio obtained from transfection of positive control. Data were normalized to the best fit values of CP-55,940 from each individual experiment before being pooled across replicates. If CP-55,940 had no response, data were left unnormalized and  $uBRET$  was used for plotting. The data were analyzed using the four-parameter logistic non-linear regression model in GraphPad Prism 9.1 and data were presented as means  $\pm$  CIs of 1-4 independent experiments.

For relative efficacy calculations for ‘**1066** and ‘**3234** versus CP-55940, first  $E_{max}$  and  $EC_{50}$  values were determined from dose-response curves to calculate the  $\log(E_{max}/EC_{50})$  value for each pathway and each compound. Then, the difference between the  $\log(E_{max}/EC_{50})$  values was calculated using the following equation:

$$\Delta \log \left( \frac{E_{max}}{EC_{50}} \right) = \log \left( \frac{E_{max}}{EC_{50}} \right)_{compound} - \log \left( \frac{E_{max}}{EC_{50}} \right)_{CP-55,940}$$

The compounds’ efficacy toward each pathway, relative to CP-55,940, were finally calculated using the following equation:

$$Relative\ Efficacy\ (RE) = 10^{\Delta \log \left( \frac{E_{max}}{EC_{50}} \right)}$$

**Bimane Fluorescence.** A minimal cysteine version of CB1 was generated<sup>65</sup> where all the cysteine residues (except C256 and C264) were mutated to alanine. A cysteine residue was engineered at residue 336 (L6.28) on TM6, which was labeled with

monobromobimane (bimane) by incubating 10  $\mu$ M receptor with 10-molar excess of bimane at room temperature for one hour. Excess label was removed using size exclusion chromatography on a Superdex 200 10/300 Increase column in 20 mM HEPES pH 7.5, 100 mM NaCl and 0.01% MNG/0.001% CHS. Bimane-labeled CB1 at 0.1 mM was incubated with ligands (10  $\mu$ M) for one hour at room temperature. Fluorescence data was collected at room temperature in a 150  $\mu$ L cuvette with a *FluorEssence v3.8 software* on a Fluorolog instrument (*Horiba*) in photon-counting mode. Bimane fluorescence was measured by excitation at 370 nm with excitation and emission bandwidth passes of 4 nm. The emission spectra were recorded from 410 to 510 nm with 1 nm increment and 0.1 s integration time.

**GTP turnover assay.** Analysis of GTP turnover was performed by using a modified protocol of the GTPase-Glo<sup>TM</sup> assay (Promega) described previously<sup>66</sup>. Ligand-bound (10  $\mu$ M ligand incubated for one hour at room temperature) or apo CB1 (1  $\mu$ M) was mixed with G-protein (1  $\mu$ M) in 20 mM HEPES, pH 7.5, 50 mM NaCl, 0.01% L-MNG/0.001% CHS, 100  $\mu$ M TCEP, 10  $\mu$ M GDP and 10  $\mu$ M GTP and incubated at room temperature. GTPase-Glo-reagent was added to the sample after incubation for 60 minutes ( $G_{i1-3}$ ) and 20 minutes for ( $G_o$ ). Luminescence was measured after the addition of detection reagent and incubation for 10 min at room temperature using a *SpectraMax Paradigm* plate reader.

### **Colloidal Aggregation Counter-Screens.**

**Dynamic Light Scattering (DLS).** Samples were prepared as 8-point half-log dilutions in filtered 50 mM KPi buffer, pH 7.0 with final DMSO concentration at 1% (v/v).

Colloidal particle formation was measured using DynaPro Plate Reader II (Wyatt Technologies). All compounds were screened in triplicate.

**Enzyme Inhibition Counter-Screening Assays.** Enzyme inhibition assays to test for colloidal inhibition were performed at room temperature using CLARIOstar Plate Reader (BMG Labtech). Samples were prepared in 50 mM KPi buffer, pH 7.0 with final DMSO concentration at 1% (v/v). Compounds were incubated with 2 nM AmpC  $\beta$ -lactamase (AmpC) or Malate dehydrogenase (MDH) for 5 minutes. AmpC reactions were initiated by the addition of 50  $\mu$ M CENTA chromogenic substrate (219475, Calbiochem). The change in absorbance was monitored at 405 nm for CENTA (219475, Calbiochem) or 490 for Nitrocefin (484400, Sigma Aldrich) for 60 sec. MDH reactions were initiated by the addition of 200  $\mu$ M nicotinamide adenine dinucleotide (NADH) (54839, Sigma Aldrich) and 200  $\mu$ M oxaloacetic acid (324427, Sigma Aldrich). The change in absorbance was monitored at 340 nm for 60 sec. Initial rates were divided by the DMSO control rate to determine % enzyme activity. Each compound was screened at 100 $\mu$ M in triplicate for three independent experiments, if enzyme inhibition greater than 30% was observed, 8-point half-log concentrations were performed in triplicate for three independent experiments. Data was analyzed using GraphPad Prism software version 9.1 (San Diego, CA).

## **Cryo-EM sample preparation and structure determination**

**Purification of hCB1.** hCB1R was expressed and purified as described previously<sup>18</sup>. An N-terminal FLAG tag and C-terminal histidine tag was added to human

full-length CB1. This CB1 construct was expressed in *Spodoptera frugiperda* Sf9 insect cells with the baculovirus method (Expression Systems). Insect cell pellets expressing CB1 was solubilized with buffer containing 1% lauryl maltose neopentyl glycol (L-MNG) and 0.1% cholesterol hemisuccinate (CHS) and purified by nickel-chelating Sepharose chromatography. The Ni column eluant was applied to a M1 anti-FLAG immunoaffinity resin. After washing to progressively decreasing concentration of L-MNG, the receptor was eluted in a buffer consisting of 20 mM HEPES pH 7.5, 150 mM NaCl, 0.05% L-MNG, 0.005% CHS, FLAG peptide and 5 mM EDTA. As the final purification step, CB1 was applied to a Superdex 200 10/300 gel filtration column (GE) in 20 mM HEPES pH 7.5, 150 mM NaCl, 0.02% L-MNG, 0.002% CHS. Ligand-free CB1 was concentrated to ~500  $\mu$ M and stored in -80 °C.

**Expression and purification of  $G_{i/o}$  heterotrimer.** Expression and purification of all heterotrimeric G-protein ( $G_{i/o}$ ) follow similar protocols. Heterotrimeric  $G_i$  was expressed and purified as previously described<sup>67</sup>. Wild-type human  $G\alpha_{i1}$  subunit virus and wild-type human  $\beta_1\gamma_2$  (with histidine tagged  $\beta$  subunit) virus were used to co-infect Insect (*Trichoplusia ni*, Hi5) cells. Cells expressing the heterotrimeric,  $G_i\beta_1\gamma_2$  G-protein were lysed in hypotonic buffer and G-protein was extracted in a buffer containing 1% sodium cholate and 0.05% n-dodecyl- $\beta$ -D-maltoside (DDM, Anatrace). Detergent was exchanged from cholate/DDM to DDM on Ni Sepharose column. The eluant from the Ni column was dialyzed overnight into 20 mM HEPES, pH 7.5, 100 mM sodium chloride, 0.1% DDM, 1 mM magnesium chloride, 100  $\mu$ M TCEP and 10  $\mu$ M GDP together with Human rhinovirus 3C protease (3C protease) to cleave off the His tag in the  $\beta$  subunit. 3C protease was

removed by Ni-chelating sepharose and the heterotrimeric G-protein was further purified with MonoQ 10/100 GL column (GE Healthcare). Protein was bound to the column and washed in buffer A (20 mM HEPES, pH 7.5, 50 mM sodium chloride, 1 mM magnesium chloride, 0.05% DDM, 100  $\mu$ M TCEP, and 10  $\mu$ M GDP). The protein was eluted with a linear gradient of 0–50% buffer B (buffer A with 1 M NaCl). The collected G protein was dialyzed into 20 mM HEPES, pH 7.5, 100 mM sodium chloride, 1 mM magnesium chloride, 0.02% DDM, 100  $\mu$ M TCEP, and 10  $\mu$ M GDP. Protein was concentrated to about 200  $\mu$ M and flash frozen until further use.

**Purification of scFv16.** scFv16 was purified with a hexahistidine-tag in the secreted form from *Trichoplusia ni* Hi5 insect cells using the baculoviral method. The supernatant from baculoviral infected cells was pH balanced and quenched with chelating agents and loaded onto Ni resin. After washing with 20 mM HEPES pH 7.5, 500 mM NaCl, and 20 mM imidazole, protein was eluted with 250 mM imidazole. Following dialysis with 3C protease into a buffer consisting of 20 mM HEPES pH 7.5 and 100 mM NaCl, scFv16 was further purified by reloading over Ni a column. The collected flow-through was applied onto a Superdex 200 16/60 column and the peak fraction was collected, concentrated and flash frozen.

**CB1-G<sub>i1</sub> complex formation and purification.** CB1 in L-MNG was incubated with excess ‘1066 for ~ 1 hour at room temperature. Simultaneously, G<sub>i1</sub> heterotrimer in DDM was incubated with 1% L-MNG/0.1% CHS at 4 °C. The ‘1066-bound CB1 was incubated with a 1.25 molar excess of detergent exchanged G<sub>i</sub> heterotrimer at room temperature for

~ 3 hour. The complex sample was further incubated with apyrase for 1.5 hour at 4 °C to stabilize a nucleotide-free complex. 2 mM CaCl<sub>2</sub> was added to the sample and purified by M1 anti-FLAG affinity chromatography. After washing to remove excess G protein and reduce detergents, the complex was eluted in 20mM HEPES pH 7.5, 100mM NaCl, 0.01% L-MNG/0.001% CHS, 0.0033% GDN/0.00033% CHS, 10 μM '1066, 5 mM EDTA, and FLAG peptide. The complex was supplemented with 100 μM TCEP and incubated with 2 molar excess of scFv16 overnight at 4 °C. Size exclusion chromatography (Superdex 200 10/300 Increase) was used to further purify the CB1-G<sub>i</sub>-scFv16 complex. The complex in 20mM HEPES pH 7.5, 100mM NaCl, 10 μM '1066, 0.00075% L-MNG/0.000075% CHS and 0.00025% GDN/0.000025% CHS was concentrated to ~12 mg/mL for electron microscopy studies.

**Cryo-EM data acquisition.** Grids were prepared by applying 3 μL of purified CB1-G<sub>i</sub> complex at 12 mg/ml to glow-discharged holey carbon gold grids (Quantifoil R1.2/1.3, 200 mesh). The grids were blotted using a Vitrobot Mark IV (FEI) with 3 s blotting time and blot force 3 at 100% humidity at room temperature and plunge-frozen in liquid ethane. A total of 8324 movies were recorded on a Titan Krios electron microscope (Thermo Fisher Scientific- FEI) operating at 300 kV at a calibrated magnification of 96,000x corresponding to a pixel size of 0.8521 Å. Micrographs were recorded using a K3 Summit direct electron camera (Gatan Inc.) with a dose rate of 16.4 electrons/pixel/s. The total exposure time was 2.5 s with an accumulated dose of ~ 56.6 electrons per Å<sup>2</sup> and a total of 50 frames per micrograph. Automatic data acquisition was done using *SerialEM*.



**Image processing and 3D reconstructions.** Micrographs were subjected to beam-induced motion correction using *MotionCor2*<sup>68</sup> implemented in Relion 2.1.0<sup>69</sup>. CTF parameters for each micrograph were determined by *CTFFIND4*<sup>70</sup>. An initial set of 4,967,593 particle projections were extracted using semi-automated procedures and subjected to reference-free two-dimensional and multiple rounds of three-dimensional classification in *Relion 2.1.0*<sup>69</sup> to remove low-resolution and otherwise poor-quality particles. From this step, 750,496 particle projections were selected for further processing in *CryoSPARC*<sup>71</sup>. A final two-dimensional classification step in order to select for the highest-resolution particles resulted in a particle set containing 465,411 particles. These particles were reconstructed to a global nominal resolution of 3.3 Å (**Extended Data Fig. 5**) at FSC of 0.143 using non-uniform refinement. Local resolution was estimated within *CryoSPARC*<sup>71</sup>.

**Model building and refinement.** The initial template of CB1 was the MDMB-Fubinaca-bound CB1-Gi complex structure (PDB: 6N4B). *Phenix.elbow* was used to generate Agonist coordinates and geometry restraints. Models were docked into the EM density map using *UCSF Chimera*. *Coot* was used for iterative model building and the final model was subjected to global refinement and minimization in real space using *phenix.real\_space\_refine* in *Phenix*. Model geometry was evaluated using *Molprobit*. FSC curves were calculated between the resulting model and the half map used for refinement as well as between the resulting model and the other half map for cross-validation (**Extended Data Fig. 5**). The final refinement parameters are provided in

**Supplementary Table 3.** The ligand symmetry accounted RMSD between the docked pose and cryo-EM pose of ‘**1066**’ was calculated by the Hungarian algorithm in DOCK6<sup>72</sup>.

## Off-target activity

**GPCRome and Comprehensive Binding Panel.** Compound ‘**3234**’ was tested at 10  $\mu$ M for off-target activity against a panel of 320 non-olfactory GPCRs using PRESTO-Tango GPCRome arrestin-recruitment assay, as described<sup>64</sup>. Receptors with at least three-fold increased relative luminescence over corresponding basal activity are potential positive hits, and were tested in dose response follow-up studies. Compound ‘**3234**’ was further tested at 1  $\mu$ M for off-target activity at a panel of 45 common GPCR and non-GPCR drug targets. Receptors with at least 50% displaced radioligand are potential positive hits and were tested in dose response follow-up studies. Screening was performed by the National Institutes of Mental Health Psychoactive Drug Screen Program (PDSP)<sup>73</sup>. Detailed experimental protocols are available on the NIMH PDSP website at <https://pdsp.unc.edu/pdspweb/content/PDSP%20Protocols%20II%202013-03-28.pdf>.

## *In vivo* methods

**Animals and ethical compliance.** Animal experiments were approved by the UCSF Institutional Animal Care and Use Committee and were conducted in accordance with the NIH Guide for the Care and Use of Laboratory animals (protocol #AN195657). Adult (8-10 weeks old) male C56BL/6 (strain # 664) and CB2R knockout (strain #5786) mice were purchased from the Jackson Laboratory. Mice were housed in cages on a standard 12:12 hour light/dark cycle with food and water ad libitum. Sample sizes were modelled on our previous studies and on studies using a similar approach, which were

able to detect significant changes<sup>74,75</sup>. The animals were randomly assigned to treatment and control groups. Animals were initially placed into one cage and allowed to freely run for a few minutes. Then each animal was randomly picked up, injected with compound treatment or vehicle, and placed into a separate cylinder before the behavioral test.

***In vivo* compound preparation.** Ligands were sourced from Enamine ('**3234**) or Sigma-Aldrich (CP-55,940, Cat No. C1112; Haloperidol, Cat. No. H1512; AM251, Cat. No. A6226; SR 144528, Cat. No. SML1899) and dissolved 30 min before injections. '**3234** was resuspended in a 20% Kolliphor HS-15 (Sigma-Aldrich, Cat. No. 42966) / 40% saline / 40% water for injections (v/v/v) vehicle for i.p. injections. CP-55,940, SR 144528, and AM251 for i.p. injections and '**3234** for i.t. injections were resuspended in a 5% EtOH /5% Kolliphor-EL (Sigma-Aldrich Cat. No. C5135) / 90% water for injections vehicle. Morphine (provided by the NIH) was resuspended in 100% saline. Haloperidol was resuspended in 20% cyclodextrin (Sigma-Aldrich, Cat. No. H107). All cannabinoid formulations were prepared in silanized glass vials.

**Pharmacokinetics.** Pharmacokinetic experiments were performed by Bienta (Enamine Biology Services) in accordance with Enamine pharmacokinetic study protocols and Institutional Animal Care and Use Guidelines (protocol number 1-2/2020). Plasma, brain, and CSF concentrations were measured for '**3234** following a 0.2 mg/kg intraperitoneal (i.p.) dose, respectively. All test compounds were formulated in Kolliphor HS – saline – water for injections (20%:40%:40%). The batches of working formulations were prepared 5-10 minutes prior to the *in vivo* study. In each compound study, up to nine

time points (5, 15, 30, 60, 120, 240, 360, 480 and 1440 min) were collected; each of the time point treatment groups included 3 male CD-1 mice. There was also a one mouse control group. All animals were fasted for 4 h before dosing. Mice were injected i.p. with 2,2,2-tribromoethanol at the dose of 150 mg/kg prior to drawing CSF and blood. Blood collection was performed from the orbital sinus in microtainers containing K2EDTA. CSF was collected under a stereomicroscope from cisterna magna using 1 ml syringes. Animals were sacrificed by cervical dislocation after the blood samples collection. After this, right lobe brain samples were collected and weighted. All samples were immediately processed, flash-frozen and stored at -70°C until subsequent analysis.

Plasma samples (40 µL) were mixed with 200 µL of IS solution. After mixing by pipetting and centrifuging for 4 min at 6,000 rpm, supernatant was injected into LC-MS/MS system. Solution of Difenoconazole (50 ng/ml in water-methanol mixture 1:9, v/v) was used as the internal standard (IS) for quantification of **'3234**. Brain samples (weight 59 mg – 179 mg) were homogenized with 5 volumes of IS(80) solution using zirconium oxide beads (115 mg ± 5 mg) in The Bullet Blender® homogenizer for 30 seconds at speed 8. After this, the samples were centrifuged for 4 min at 14,000 rpm, and supernatant was injected into LC-MS/MS system. CSF samples (4 µL) were mixed with 100 µL of IS(80) solution. After mixing by pipetting and centrifuging for 4 min at 6,000 rpm, 6 µl of each supernatant was injected into LC-MS/MS system.

Analyses of plasma, brain and CSF samples were conducted at Enamine/Bienta. The concentrations of compounds in samples were determined using high performance

liquid chromatography/tandem mass spectrometry (HPLC-MS/MS) method. Data acquisition and system control was performed using Analyst 1.6.3 software (AB Sciex, Canada). The concentrations of the test compound below the lower limit of quantitation (LLOQ for **'3234**: 2 ng/ml for plasma, 1 ng/g for brain; 2.5 ng/ml for CSF samples) were designated as zero. The pharmacokinetic data analysis was performed using noncompartmental, bolus injection or extravascular input analysis models in WinNonlin 5.2 (PharSight). Data below LLOQ were presented as missing to improve validity of  $T_{1/2}$  calculations.

**Behavioral analyses.** For all behavioral tests, the experimenter was always blind to treatment. Animals were first habituated for 30-60 minutes in Plexiglas cylinders and then tested 30 minutes after i.p. or i.t. injection of the compounds. The mechanical (von Frey), thermal (Hargreaves, and tail flick) and ambulatory (rotarod) tests were conducted as described<sup>76</sup>. Hindpaw mechanical thresholds were determined with von Frey filaments using the up-down method<sup>77</sup>. Hindpaw thermal sensitivity was measured with a radiant heat source (Hargreaves). For the tail flick assay, sensitivity was measured by immersing the tail into a 50°C water bath. For the ambulatory (rotarod) test, mice were first trained on an accelerating rotating rod, three times for 5 min, before testing with any compound. Therapeutic index was calculated as the ratio of the minimum dose of side effect phenotype and the minimum dose of analgesic phenotype.

**SNI model of neuropathic pain.** Under isoflurane anesthesia, two of the three branches of the sciatic nerve were ligated and transected distally<sup>78</sup>, leaving the sural nerve intact. Behavior was tested 7 to 14 days after injury.

**CFA.** The CFA model of chronic inflammation was induced as described previously<sup>79</sup>. Briefly, CFA (Sigma) was diluted 1:1 with saline and vortexed for 30 min. When fully suspended, we injected 20 µL of CFA into one hindpaw. Heat thresholds were measured before the injection (baseline) and 3 days after the injection using the Hargreaves test.

**Open Field Test.** Thirty minutes after IP injection, mice were placed in the center of a round open-field (2 feet diameter) and their exploratory behavior recorded over the next 15 minutes. Distance traveled, mean speed as well as percent time spent in the center were calculated.

**Conditioned Place Preference.** To determine if ‘**3234**’ was inherently rewarding or aversive we used the conditioned place paradigm as described<sup>80</sup>. Briefly, mice were first habituated to the test apparatus, twice, and their preference for each chamber recorded for 30 minutes (Pretest). Two conditioning days followed in which mice received the vehicle control or the compound, and 30 minutes later restricted for 30 minutes in the preferred or non-preferred chamber, respectively. On day 5 (Test day), mice were allowed to roam freely between the 3 chambers of the apparatus and their preference for each chamber recorded for 30 minutes. To calculate the CPP score, we subtracted the time

spent in each chamber of the box on the Pretest day from that of the Test day (CPP score = Test - Pretest).

**Acetone Test.** Mice were placed on a wire mesh and thirty min after an IP injection of the compounds we applied a drop (50  $\mu$ L) of acetone on the ventral aspect of the hindpaw, 5 times every 30 sec. We recorded the number of nocifensive behaviors (paw lifts/licks/shakes/bites) over the 5 applications.

**Formalin Test.** Thirty minutes after an IP injection of the compounds, mice received an intraplantar injection of a 20 $\mu$ l solution containing 2% formalin (Acros Organics) and we recorded the time mice spent licking/biting/guarding (nocifensive behaviors) the injected hindpaw over the next 60 min.

**Catalepsy Test.** Thirty and 60 minutes after an IP injection of the compounds, mice were placed on a vertical wire mesh and the latency to move all four paws was recorded.

**Temperature measurements.** Mice were shaved at the nape of the neck to expose skin. The next day, mice were placed in cylinders for 15 minutes and then received an IP injection of the compounds. Thirty and 60 minutes later, we recorded the temperature of the skin at the nape of the neck using an infrared dual laser thermometer (Thomas Scientific). The average was calculated from 3 measurements taken 1 min apart.



**Statistical analyses.** All statistical tests were run with GraphPad Prism 9.0 (GraphPad Software Inc., San Diego). A two-tailed unpaired *t*-test was used to compare the  $pK_i \pm \text{SEM}$  for '3234 at CB1 versus CB2 (**Extended Data Fig. 8** legend). Experiments of the compounds in the in vivo assays were analyzed by unpaired two-tailed *t*-tests, one-way ANOVA, or two-way ANOVA, depending on the experimental design. All statistical calculations were controlled for multiple hypothesis testing using a post-hoc test as described in the **Fig. 5** or **Extended Data Fig. 10** legends. Details of the analyses, including groups compared in post-hoc sets, number of animals per group, *t* or *F* statistics, and *P* values, can be found in the figure legends.

**Data availability.** The structure described in this manuscript were deposited to the Protein Data Bank under accession code 8GAG, and the map coordinates to EMDB under accession code EMD-29898. Additional data provided in the main text, extended data, or supplemental materials. Additional requests can be made to the corresponding authors.

**Code availability.** DOCK3.7 is freely available for non-commercial research in both executable and code form (<http://dock.compbio.ucsf.edu/DOCK3.7/>). A web-based version is freely available to all (<http://blaster.docking.org/>). The ultra-large library used here is freely available (<http://zinc15.docking.org>, <http://zinc20.docking.org>).

## References

1. Lipman, A. G. Medical cannabis for pain: anecdote or evidence. *J. Pain Palliat. Care Pharmacother.* **31**, 96–97 (2017).
2. Iliopoulos-Tsoutsouvas, C., Georgiadis, M.-O., Ji, L., Nikas, S. P. & Makriyannis, A. New tools to interrogate endocannabinoid signalling: from natural compounds to synthetic drugs. in *New tools to interrogate endocannabinoid signaling* (Ed. Maccarrone, M.) 48–88 (Royal Society of Chem., 2020).
3. Sachs, J., McGlade, E. & Yurgelun-Todd, D. Safety and toxicology of cannabinoids. *Neurotherapeutics* **12**, 735–746 (2015).
4. Cohen, K., Weizman, A. & Weinstein, A. Positive and negative effects of cannabis and cannabinoids on health. *Clin Pharmacol Ther* **105**, 1139–1147 (2019).
5. Donvito, G. *et al.* The endogenous cannabinoid system: a budding source of targets for treating inflammatory and neuropathic pain. *Neuropsychopharmacol.* **43**, 52–79 (2018).
6. Papagianni, E. P. & Stevenson, C. W. Cannabinoid regulation of fear and anxiety: an update. *Curr. Psychiat. Rep.* **21**, 38 (2019).
7. Rock, E. M. & Parker, L. A. Cannabinoids as potential treatment for chemotherapy-induced nausea and vomiting. *Front. Pharmacol.* **7**, 221 (2016).
8. Rossi, F., Punzo, F., Umamo, G. R., Argenziano, M. & Giudice, E. M. D. Role of cannabinoids in obesity. *Int. J Mol. Sci.* **19**, 2690 (2018).
9. Perucca, E. Cannabinoids in the treatment of epilepsy: hard evidence at last? *J. Epilepsy Res.* **7**, 61–76 (2017).

10. Banister, S. D., Kumar, K. K., Kumar, V., Kobilka, B. K. & Malhotra, S. V. Selective modulation of the cannabinoid type 1 (CB1) receptor as an emerging platform for the treatment of neuropathic pain. *Medchemcomm* **10**, 647–659 (2019).
11. Martin, B. R. *et al.* Behavioral, biochemical, and molecular modeling evaluations of cannabinoid analogs. *Pharmacol. Biochem. Be.* **40**, 471–478 (1991).
12. Fisher, E. *et al.* Cannabinoids, cannabis, and cannabis-based medicine for pain management: a systematic review of randomised controlled trials. *Pain* **162**, S45–S66 (2021).
13. Finn, D. P. *et al.* Cannabinoids, the endocannabinoid system, and pain: a review of preclinical studies. *Pain* **162**, S5–S25 (2021).
14. Pertwee, R. G. The diverse CB1 and CB2 receptor pharmacology of three plant cannabinoids:  $\Delta^9$ -tetrahydrocannabinol, cannabidiol and  $\Delta^9$ -tetrahydrocannabivarin. *Brit. J. Pharmacol.* **153**, 199–215 (2008).
15. Hua, T. *et al.* Crystal structure of the human cannabinoid receptor CB1. *Cell* **167**, 750–762 (2016).
16. Hua, T. *et al.* Crystal structures of agonist-bound human cannabinoid receptor CB1. *Nature* **547**, 468–471 (2017).
17. Shao, Z. *et al.* High-resolution crystal structure of the human CB1 cannabinoid receptor. *Nature* **540**, 602–606 (2016).
18. Kumar, K. K. *et al.* Structure of a signaling cannabinoid receptor 1-G protein complex. *Cell* 448–458 (2019).
19. Hua, T. *et al.* Activation and signaling mechanism revealed by cannabinoid receptor-Gi complex structures. *Cell* **180**, 655–665 (2020).

20. Xing, C. *et al.* Cryo-EM Structure of the human cannabinoid receptor CB2-Gi signaling complex. *Cell* **180**, 645-654 (2020).
21. Li, X. *et al.* Crystal structure of the human cannabinoid receptor CB2. *Cell* **176**, 459-467 (2019).
22. Lyu, J. *et al.* Ultra-large library docking for discovering new chemotypes. *Nature* **566**, 224–229 (2019).
23. Alon, A. *et al.* Structures of the  $\sigma$ 2 receptor enable docking for bioactive ligand discovery. *Nature* **600**, 759–764 (2021).
24. Sadybekov, A. A. *et al.* Synthon-based ligand discovery in virtual libraries of over 11 billion compounds. *Nature* **601**, 452–459 (2022).
25. Stein, R. M. *et al.* Virtual discovery of melatonin receptor ligands to modulate circadian rhythms. *Nature* **579** 609–614 (2020).
26. Fink, E. A. *et al.* Structure-based discovery of nonopioid analgesics acting through the  $\alpha$ 2A-adrenergic receptor. *Science* **377**, eabn7065 (2022).
27. Manglik, A. *et al.* Structure-based discovery of opioid analgesics with reduced side effects. *Nature* **537**, 185 (2016).
28. Gorgulla, C. *et al.* An open-source drug discovery platform enables ultra-large virtual screens. *Nature* **580**, 663–668 (2020).
29. Lipinski, C. A., Lombardo, F., Dominy, B. W. & Feeney, P. J. Experimental and computational approaches to estimate solubility and permeability in drug discovery and development settings. *Adv. Drug Deliver. Rev.* **23**, 3–25 (1997).
30. Sterling, T. & Irwin, J. J. ZINC 15 – ligand discovery for everyone. *J. Chem. Inf. Model* **55**, 2324–2337 (2015).

31. Gaulton, A. *et al.* ChEMBL: a large-scale bioactivity database for drug discovery. *Nucleic Acids Res.* **40**, D1100–D1107 (2012).
32. Bento, A. P. *et al.* The ChEMBL bioactivity database: an update. *Nucleic Acids Res.* **42**, D1083–D1090 (2014).
33. Ballesteros, J. A. & Weinstein, H. Integrated methods for the construction of three-dimensional models and computational probing of structure-function relations in G protein-coupled receptors. *Methods Neurosci.* **25**, 366–428 (1995).
34. Pettersen, E. F. *et al.* UCSF Chimera—A visualization system for exploratory research and analysis. *J. Comput. Chem.* **25**, 1605–1612 (2004).
35. Kapur, A. *et al.* Mutation Studies of Ser7.39 and Ser2.60 in the human CB1 cannabinoid receptor: evidence for a serine-induced bend in CB1 transmembrane helix 7. *Mol. Pharmacol.* **71**, 1512–1524 (2007).
36. McAllister, S. D. *et al.* Structural mimicry in class A G protein-coupled receptor rotamer toggle switches: the importance of the F3.36(201)/W6.48(357) interaction in cannabinoid CB1 receptor activation. *J. Biol. Chem.* **279**, 48024–48037 (2004).
37. Ramesh, K. & Rosenbaum, D. M. Molecular basis for ligand modulation of the cannabinoid receptor CB1. *Brit. J. Pharmacol.* **179**, 3487–3495 (2021).
38. Kolb, P. *et al.* Community guidelines for GPCR ligand bias: IUPHAR review 32. *Brit. J. Pharmacol.* **179**, 3651–3674 (2022).
39. Avet, C. *et al.* Effector membrane translocation biosensors reveal G protein and  $\beta$ arrestin coupling profiles of 100 therapeutically relevant GPCRs. *Elife* **11**, e74101 (2022).

40. Manning, J. J., Green, H. M., Glass, M. & Finlay, D. B. Pharmacological selection of cannabinoid receptor effectors: signalling, allosteric modulation and bias. *Neuropharmacology* **193**, 108611 (2021).
41. Martin, W. J., Loo, C. M. & Basbaum, A. I. Spinal cannabinoids are anti-allodynic in rats with persistent inflammation. *Pain* **82**, 199–205 (1999).
42. Fox, A. *et al.* The role of central and peripheral cannabinoid-1 receptors in the antihyperalgesic activity of cannabinoids in a model of neuropathic pain. *Pain* **92**, 91–100 (2001).
43. Sain, N. M. H., Liang, A., Kane, S. A. & Urban, M. O. Antinociceptive effects of the non-selective cannabinoid receptor agonist CP 55,940 are absent in CB1<sup>-/-</sup> and not CB2<sup>-/-</sup> mice in models of acute and persistent pain. *Neuropharmacology* **57**, 235–241 (2009).
44. Tham, S. M., Angus, J. A., Tudor, E. M. & Wright, C. E. Synergistic and additive interactions of the cannabinoid agonist CP55,940 with  $\mu$  opioid receptor and  $\alpha$ 2-adrenoceptor agonists in acute pain models in mice. *Brit. J. Pharmacol.* **144**, 875–884 (2005).
45. Grenald, S. A. *et al.* Synergistic attenuation of chronic pain using mu opioid and cannabinoid receptor 2 agonists. *Neuropharmacology* **116**, 59–70 (2017).
46. Vlachou, S. & Panagis, G. Regulation of brain reward by the endocannabinoid system: a critical review of behavioral studies in animals. *Curr. Pharm. Design* **20**, 2072–2088 (2014).
47. Schmid, C. L. *et al.* Bias factor and therapeutic window correlate to predict safer opioid analgesics. *Cell* **171**, 1165–1175 (2017).

48. Beckers, M., Fechner, N. & Stiefl, N. 25 Years of small-molecule optimization at Novartis: a retrospective analysis of chemical series evolution. *J. Chem. Inf. Model* **62**, 6002–6021 (2022).
49. Meng, E. C., Shoichet, B. K. & Kuntz, I. D. Automated docking with grid-based energy evaluation. *J. Comput. Chem.* **13**, 505–524 (1992).
50. Weiner, S. J. *et al.* A new force field for molecular mechanical simulation of nucleic acids and proteins. *J. Am. Chem. Soc.* **106**, 765–784 (1984).
51. Gallagher, K. & Sharp, K. Electrostatic contributions to heat capacity changes of DNA-ligand binding. *Biophys. J.* **75**, 769–776 (1998).
52. Mysinger, M. M. & Shoichet, B. K. Rapid context-dependent ligand desolvation in molecular docking. *J. Chem. Inf. Model.* **50**, 1561–1573 (2010).
53. Kuntz, I. D., Blaney, J. M., Oatley, S. J., Langridge, R. & Ferrin, T. E. A geometric approach to macromolecule-ligand interactions. *J. Mol. Biol.* **161**, 269–288 (1982).
54. Word, J. M., Lovell, S. C., Richardson, J. S. & Richardson, D. C. Asparagine and glutamine: using hydrogen atom contacts in the choice of side-chain amide orientation. *J. Mol. Biol.* **285**, 1735–1747 (1999).
55. Bender, B. J. *et al.* A practical guide to large-scale docking. *Nat. Protoc.* **16**, 4799–4832 (2021).
56. Southan, C. *et al.* The IUPHAR/BPS guide to pharmacology in 2016: towards curated quantitative interactions between 1300 protein targets and 6000 ligands. *Nucleic. Acids Res.* **44**, D1054–D1068 (2016).
57. Stein, R. M. *et al.* Property-unmatched decoys in docking benchmarks. *J. Chem. Inf. Model* **61**, 699–714 (2021).



58. Shoichet, B. K., Leach, A. R. & Kuntz, I. D. Ligand solvation in molecular docking. *Proteins Struct. Funct. Bioinform.* **34**, 4–16 (1999).
59. Mysinger, M. M. *et al.* Structure-based ligand discovery for the protein–protein interface of chemokine receptor CXCR4. *Proc. National Acad. Sci.* **109**, 5517–5522 (2012).
60. Coleman, R. G., Carchia, M., Sterling, T., Irwin, J. J. & Shoichet, B. K. Ligand pose and orientational sampling in molecular docking. *Plos One* **8**, e75992 (2013).
61. Tolmachev, A. *et al.* Expanding synthesizable space of disubstituted 1,2,4-oxadiazoles. *ACS Comb. Sci.* **18**, 616–624 (2016).
62. Janero, D. R. *et al.* Molecular-interaction and signaling profiles of AM3677, a novel covalent agonist selective for the cannabinoid 1 receptor. *ACS Chem. Neurosci.* **6**, 1400–1410 (2015).
63. Pryce, K. D. *et al.* A promising chemical series of positive allosteric modulators of the  $\mu$ -opioid receptor that enhance the antinociceptive efficacy of opioids but not their adverse effects. *Neuropharmacology* **195**, 108673 (2021).
64. Kroeze, W. K. *et al.* PRESTO-Tango as an open-source resource for interrogation of the druggable human GPCRome. *Nat. Struct. Mol. Biology* **22**, 362–369 (2015).
65. Fay, J. F. & Farrens, D. L. The Membrane proximal region of the cannabinoid receptor CB1 N-terminus can allosterically modulate ligand affinity. *Biochemistry* **52**, 8286–8294 (2013).
66. Gregorio, G. G. *et al.* Single-molecule analysis of ligand efficacy in  $\beta$ 2AR–G-protein activation. *Nature* **547**, 68–73 (2017).

67. Dror, R. O. *et al.* Structural basis for nucleotide exchange in heterotrimeric G proteins. *Science* **348**, 1361–1365 (2015).
68. Zheng, S. Q. *et al.* MotionCor2: anisotropic correction of beam-induced motion for improved cryo-electron microscopy. *Nat. Methods* **14**, 331–332 (2017).
69. Fernandez-Leiro, R. & Scheres, S. H. W. A pipeline approach to single-particle processing in RELION. *Acta Crystallogr. Sect. D* **73**, 496–502 (2017).
70. Rohou, A. & Grigorieff, N. CTFFIND4: Fast and accurate defocus estimation from electron micrographs. *J. Struct. Biol.* **192**, 216–221 (2015).
71. Punjani, A., Rubinstein, J. L., Fleet, D. J. & Brubaker, M. A. cryoSPARC: algorithms for rapid unsupervised cryo-EM structure determination. *Nat. Methods* **14**, 290–296 (2017).
72. Allen, W. J. & Rizzo, R. C. Implementation of the hungarian algorithm to account for ligand symmetry and similarity in structure-based design. *J. Chem. Inf. Model* **54**, 518–529 (2014).
73. Besnard, J. *et al.* Automated design of ligands to polypharmacological profiles. *Nature* **492**, 215 (2012).
74. Scherrer, G. *et al.* Dissociation of the opioid receptor mechanisms that control mechanical and heat pain. *Cell* **137**, 1148–1159 (2009).
75. Muralidharan, A. *et al.* Identification and characterization of novel candidate compounds targeting 6- and 7-transmembrane  $\mu$ -opioid receptor isoforms. *Brit. J. Pharmacol.* **178**, 2709–2726 (2021).

76. Tran, M. *et al.* Ablation of spinal cord estrogen receptor  $\alpha$ -expressing interneurons reduces chemically induced modalities of pain and itch. *J. Comp. Neurol.* **528**, 1629–1643 (2020).
77. Chaplan, S. R., Bach, F. W., Pogrel, J. W., Chung, J. M. & Yaksh, T. L. Quantitative assessment of tactile allodynia in the rat paw. *J. Neurosci. Met.h* **53**, 55–63 (1994).
78. Shields, S. D., Eckert, W. A. & Basbaum, A. I. Spared nerve injury model of neuropathic pain in the mouse: a behavioral and anatomic analysis. *J. Pain.* **4**, 465–470 (2003).
79. Cao, Y. Q. *et al.* Primary afferent tachykinins are required to experience moderate to intense pain. *Nature* **392**, 32897 (1998).
80. Juarez-Salinas, D. L., Braz, J. M., Hamel, K. A. & Basbaum, A. I. Pain relief by supraspinal gabapentin requires descending noradrenergic inhibitory controls. *Pain Reports* **3**, e659 (2018).

**Funding.** This work is supported by DARPA grant HR0011-19-2-0020 (B.K.S., A.I.B., & J.J.I.), US NIH grant R35GM122481 (B.K.S.), US NIH grant R01GM133836 (J.J.I.), US R35NS097306 (A.I.B.), Open Philanthropy (A.I.B.), and US NIH grant P01DA009158 (A.M.).

**Acknowledgements.** We thank C. Webb for help with the initial CB1 docking screen. We thank B. Ahanou for help analyzing the open field data. We thank M. M. Rachman for editing the manuscript. We gratefully acknowledge OpenEye Software for Omega and related tools and Schrödinger, Inc. for the Maestro package. Select receptor binding profiles and agonist functional data was generously provided by the National Institute of Mental Health's Psychoactive Drug Screening Program, Contract # HHSN-271-2018-00023-C, directed by B. Roth.

**Author contributions.** T.A.T. and R.M.S. conducted the docking screens with input from B.K.S. Ligand optimization was performed by T.A.T. and C.I.-T. with input from B.K.S., and A.M.. N.G.T., S.G., F.T., and Y.L. performed binding or functional assays with input from T.A.T., C.I.-T., and A.M.. K.K. prepared the CB1-G<sub>i</sub> complex, collected cryo-EM data with help from E.S.O., and modelled the structure with help from F.L.. K.K. collected bimane data with help from Y.S.. T.A.T. and J.M.B. did the drug formulations for *in vivo* experiments. J.M.B. performed and analyzed the *in vivo* pharmacology experiments assisted by T.A.T., V.C., S.R.R., K.B., and J.B., supervised and coanalyzed by A.I.B.. E.S.O processed data and obtained the cryo-EM map. Y.S. performed the GTP-turnover assays with help from K.K. and E.S.O.. H.K. and C.N. tested select compounds

in the panel of G-protein and  $\beta$ -arrestin subtypes with supervision from M.S. and L.S.. C.I.-T. and T.C.H. synthesized bespoke compounds with supervision from A.M.. I.G. performed the colloidal aggregation screens. Y.S.M. and D.S.R. supervised compound synthesis of Enamine compounds purchased from the ZINC15 database and 12 billion catalog. J.J.I. built the ZINC15 ultra-large libraries. B.K.S., A.I.B., A.M., and K.K. supervised the project. T.A.T. wrote the paper with input from all other authors, and primary editing from B.K.S.

**Competing interests.** B.K.S. is a founder of Epiodyne, BlueDolphin and Deep Apple Therapeutics and consults in docking and in the GPCR space. J.J.I. is a cofounder of BlueDolphin and Deep Apple Therapeutics. Y.S.M. is a CEO of Chemspace LLC and a scientific advisor at Enamine, Ltd. D.S.R. is an employee of Enamine, Ltd. H.K., C.N., M.S., and L.S. are employees of Domain Therapeutics North America Inc.. The authors declare no other competing interests.

**Additional information.** Supplementary Information is available for this paper. Correspondence and requests for materials should be addressed to the corresponding authors.